(4)

AFGL-TR-88-0322

ANALYSIS OF REGIONAL PHASES USING THREE COMPONENT DATA

Michael Prange
M. Nafi Toksöz

Earth Resources Laboratory
Department of Earth, Atmospheric, and
Planetary Sciences
Massachusetts Institute of Technology
Cambridge, Massachusetts 02139

28 November 1988

Scientific Report No. 1

APPROVED FOR PUBLIC RELEASE; DISTRIBUTION UNLIMITED

Air Force Geophysics Laboratory
Air Force Systems Command
United States Air Force
Hanscom Air Force Base, Massachusetts 01731-5000

Sponsored by: Defense Advanced Research Projects Agency
Nuclear Monitoring Research Office
DARPA Order No. 5307
Monitored by: Air Force Geophysics Laboratory
Contract No. F19628-87-K-0054

"This technical report has been reviewed and is approved for publication"

JAMES F. LEWKOWICZ
Contract Manager
Solid Earth Geophysics Branch
Earth Sciences Division

JAMES F. LEWKOWICZ
Acting Chief
Solid Earth Geophysics Branch
Earth Sciences Division

FOR THE COMMANDER

DONALD H. ECKHARDT, Director
Earth Sciences Division

This document has been reviewed by the ESD Public Affairs Office (PA) and is releasable to the National Technical Information Service (NTIS).

Qualified requestors may obtain additional copies from the Defense Technical Information Center. All others should apply to the National Technical Information Service.

If your address has changed, or if you wish to be removed from the mailing list, or if the addressee is no longer employed by your organization, please notify AFGL/DAA, Hanscom AFB, MA 01731-5000. This will assist us in maintaining a current mailing list.

Do not return copies of this report unless contractual obligations or notices on a specific document requires that it be returned.

Unclassified
SECURITY CLASSIFICATION OF THIS PAGE

REPORT DOCUMENTATION PAGE

1a REPORT SECURITY CLASSIFICATION unclassified	1b RESTRICTIVE MARKINGS
2a SECURITY CLASSIFICATION AUTHORITY	3 DISTRIBUTION / AVAILABILITY OF REPORT Approved for public release; distribution unlimited
2b DECLASSIFICATION / DOWNGRADING SCHEDULE	
4 PERFORMING ORGANIZATION REPORT NUMBER(S)	5 MONITORING ORGANIZATION REPORT NUMBER(S) AFGL-TR-88-0322
6a NAME OF PERFORMING ORGANIZATION Earth Resources Laboratory Dept. of Earth, Atmospheric, and Planetary Sciences 6b OFFICE SYMBOL (If applicable)	7a NAME OF MONITORING ORGANIZATION Air Force Geophysics Laboratory
6c ADDRESS (City, State, and ZIP Code) Massachusetts Institute of Technology Cambridge, MA 02139	7b ADDRESS (City, State, and ZIP Code) Hanscom AFB, MA 01731-5000
8a NAME OF FUNDING / SPONSORING ORGANIZATION 8b OFFICE SYMBOL (If applicable)	9 PROCUREMENT INSTRUMENT IDENTIFICATION NUMBER F19628-87-K-0054
8c ADDRESS (City, State, and ZIP Code)	10 SOURCE OF FUNDING NUMBERS PROGRAM ELEMENT NO: 62714E; PROJECT NO: 7A10; TASK NO: DA; WORK UNIT ACCESSION NO: CM

11 TITLE (Include Security Classification)
Analysis of Regional Phases Using Three-Component Data

12 PERSONAL AUTHOR(S)
M. Nafi Toksoz, M. Prange

13a TYPE OF REPORT	13b TIME COVERED	14 DATE OF REPORT (Year, Month, Day)	15 PAGE COUNT
Scientific Report #1	FROM 8/19/87 TO 8/31/88	88 11 28	68

16 SUPPLEMENTARY NOTATION

17 COSATI CODES			18 SUBJECT TERMS (Continue on reverse if necessary and identify by block number)
FIELD	GROUP	SUB-GROUP	rough interface, 3d seismic scattering, reflection/ transmission coefficients

19 ABSTRACT (Continue on reverse if necessary and identify by block number)

See reverse side of page

20 DISTRIBUTION / AVAILABILITY OF ABSTRACT ☒ UNCLASSIFIED/UNLIMITED ☐ SAME AS RPT ☐ DTIC USERS	21 ABSTRACT SECURITY CLASSIFICATION unclassified
22a NAME OF RESPONSIBLE INDIVIDUAL James F. Lewkowicz	22b TELEPHONE (Include Area Code) 617/377-3028 22c OFFICE SYMBOL LWH

DD FORM 1473, 84 MAR 83 APR edition may be used until exhausted
All other editions are obsolete

SECURITY CLASSIFICATION OF THIS PAGE
Unclassified

BLOCK 19: ABSTRACT

A method is presented for computing three-dimensional seismic wave scattering from a rough interface. It is derived using a perturbation approach which requires interface height perturbations to be small relative to the wavelengths of scattered waves, and interface slope perturbations to be much less than one. These validity conditions are based on an order of error analysis of the truncation of the perturbation series. Comparison of reflection and transmission coefficients generated by the perturbation method with those generated from a second-order finite difference method for several rough interface models with Gaussian auto-correlation functions shows that the perturbation method is accurate for RMS interface height deviations of less than about a tenth of the smallest wavelength in the scattered field. This result is independent of RMS interface slope in the tested range of 0.037 to 0.99.

Three-dimensional scattering results are presented for normally incident, planar P and SV waves on a rough interface with a Gaussian auto-correlation function (RMS height is 0.125 S_1 wavelengths and RMS slope is 0.03). For the SV source, the scattering coefficients for the generated P, SV, and SH waves had maxima in the azimuth where the scattered wave particle motion coincided with the source particle motion. The maximum of the SV reflection scattering coefficient is 37 percent of the mean planar interface reflection coefficient. The P source generated P and SV waves with azimuthally symmetric scattering coefficients. The maximum of the P scattering coefficient in this case is 27 percent of mean planar interface reflection coefficient.

TABLE OF CONTENTS

Preface

The following document is a portion of the Ph.D. Thesis of Michael Prange entitled, "Perturbation Approximation of 3-D Seismic Scattering".

INTRODUCTION

The presence of a rough interface can strongly affect seismic waves reflected from and transmitted through that interface, even when the scale of roughness is much less than a wavelength. These effects include changes in the amplitude, scattering angle, frequency content, and wave-type conversion of the scattered wave. Available exact solutions take the form of integral equations (DeSanto and Brown, 1986) or finite difference/finite element formulations (Levander and Hill, 1985) that are prohibitively expensive to solve in three dimensions.

In this paper, I present a perturbation approach to the solution of the three-dimensional elastic wave equation which satisfies welded boundary conditions at a rough interface. This solution is an extension of two-dimensional surface wave scattering formulations(Kennett, 1972; Gilbert and Knopoff, 1960). The method height and slope of interface irregularities to be small with respect to the wavelengths of the elastic waves present. In order to understand the effects of rough interface scattering on body waves, we then present a method to separate the scattered field into up- and down-going P, SV and SH waves so that rough interface scattering coefficients can be calculated. To test the perturbation approximation, we compare these analytical results with finite difference solutions generated for the same rough interface models. Finally, we discuss the features of the three-dimensional scattered field.

THREE-DIMENSIONAL SCATTERING FORMULATION

A fine-scale blow-up of a three-dimensional rough interface is shown in Figure 1. The irregular interface is described by $z = h(x, y)$, and has a downward normal $\underline{n}(x, y)$. It separates an upper medium, described by P and S wave velocities α_1 and β_1 and density ρ_1, from a lower medium, described by α_2, β_2, and ρ_2. The essence of the formulation is to project displacements and stresses on the two sides of the rough interface onto a planar surface whose depth equals the mean depth of the rough interface. These projected fields are then expanded in a perturbation series in h about a background field consisting of the known planar interface solution. This procedure results in a formulation in which the rough interface scattering problem is replaced by a planar interface scattering problem, with sources along the planar interface generating the rough interface component of the scattered field.

The general form of the elastic wave equation which is valid for small displacements in the absence of body forces is

$$-\rho\omega^2 u_i = \tau_{ji,j}, \qquad i, j \in \{x, y, z\} \tag{1}$$

where u_i is the ith component of the displacement vector, τ_{ji} is the i, j component of the Cauchy stress tensor, the comma denotes differentiation in the j-th coordinate direction, ω is the temporal frequency, and the Einstein summation convention applies. Throughout this

paper, the Fourier transform in x, y, and t uses an implied phase factor of $\exp(ik_x x + ik_y y - i\omega t)$. For an isotropic solid, stresses are related to displacements by the constitutive relation

$$\tau_{ij} = \lambda u_{k,k}\delta_{ij} + \mu(u_{i,j} + u_{j,i}), \tag{2}$$

where δ_{ij} is the Kroniker symbol and λ and μ are the Lamé parameters. Equations (1) and (2) can be expressed as a 6×6 matrix wave equation in the form

$$\frac{d\underline{r}}{dz} = \underline{\underline{A}}\,\underline{r}, \tag{3}$$

where $\underline{r}$ is the displacement-stress vector defined by $\underline{r} = [u_x,\ u_y,\ u_z,\ \tau_{xz},\ \tau_{yz},\ \tau_{zz}]^T$ and $\underline{\underline{A}}$ is defined by

$$\underline{\underline{A}} = \begin{bmatrix} 0 & 0 & -\partial_x & \frac{1}{\mu} & 0 & 0 \\ 0 & 0 & -\partial_y & 0 & \frac{1}{\mu} & 0 \\ \frac{-\lambda}{\lambda+2\mu}\partial_x & \frac{-\lambda}{\lambda+2\mu}\partial_y & 0 & 0 & 0 & \frac{1}{\lambda+2\mu} \\ -\rho\omega^2 - \zeta\partial_{xx} - \mu\partial_{yy} & -\mu(1+\frac{2\lambda}{\lambda+2\mu})\partial_{xy} & 0 & 0 & 0 & \frac{-\lambda}{\lambda+2\mu}\partial_x \\ -\mu(1+\frac{2\lambda}{\lambda+2\mu})\partial_{xy} & -\rho\omega^2 - \mu\partial_{xx} - \zeta\partial_{yy} & 0 & 0 & 0 & \frac{-\lambda}{\lambda+2\mu}\partial_y \\ 0 & 0 & -\rho\omega^2 & -\partial_x & -\partial_y & 0 \end{bmatrix} \tag{4}$$

with $\zeta = 4\mu(\lambda+\mu)/(\lambda+2\mu)$.

Welded boundary conditions at the rough interface require continuity of displacement and traction at each point on the interface. These tractions must be measured with respect to a plane tangent to the interface, and are given by $T_j = \sigma_{jk}n_k$. The downward unit normal n_k is defined by

$$\begin{bmatrix} n_x \\ n_y \\ n_z \end{bmatrix} = \frac{1}{\sqrt{1 + h_{,x}^2 + h_{,y}^2}} \begin{bmatrix} -h_{,x} \\ -h_{,y} \\ 1 \end{bmatrix} \tag{5}$$

A new vector quantity which is continuous at the rough interface is defined to be

$$\begin{bmatrix} u_x \\ u_y \\ u_z \\ T_x\sqrt{1+h_{,x}^2+h_{,y}^2} \\ T_y\sqrt{1+h_{,x}^2+h_{,y}^2} \\ T_z\sqrt{1+h_{,x}^2+h_{,y}^2} \end{bmatrix} = \begin{bmatrix} 1 & 0 & 0 & 0 & 0 & 0 \\ 0 & 1 & 0 & 0 & 0 & 0 \\ 0 & 0 & 1 & 0 & 0 & 0 \\ -h_{,x}\zeta\partial_x & -h_{,x}\frac{2\lambda\mu}{\lambda+2\mu}\partial_y & 0 & 1 & 0 & h_{,x}\frac{-\lambda}{\lambda+2\mu} \\ -h_{,y}\mu\partial_y & -h_{,y}\mu\partial_x & & & & \\ -h_{,x}\mu\partial_y & -h_{,x}\mu\partial_x & 0 & 0 & 1 & h_{,y}\frac{-\lambda}{\lambda+2\mu} \\ -h_{,y}\frac{2\lambda\mu}{\lambda+2\mu}\partial_x & -h_{,y}\zeta\partial_y & & & & \\ 0 & 0 & 0 & -h_{,x} & -h_{,y} & 1 \end{bmatrix} \begin{bmatrix} u_x \\ u_y \\ u_z \\ \tau_{zz} \\ \tau_{yz} \\ \tau_{xz} \end{bmatrix} \tag{6}$$

Writing (6) in a form which explicitly expresses the h dependence, this transformation takes the form

$$\underline{\hat{r}}(h) = (\underline{\underline{I}} + h_{,x}\underline{\underline{Q}}_x + h_{,y}\underline{\underline{Q}}_y)\underline{r}(h) \tag{7}$$

where $\underline{\hat{r}}$ and $\underline{r}$ are evaluated along the rough interface, $\underline{\underline{I}}$ is the identity matrix and $\underline{\underline{Q}}_x$ and $\underline{\underline{Q}}_y$ are

$$\underline{\underline{Q}}_x = \begin{bmatrix} 0 & 0 & 0 & 0 & 0 & 0 \\ 0 & 0 & 0 & 0 & 0 & 0 \\ 0 & 0 & 0 & 0 & 0 & 0 \\ -\zeta\partial_x & \frac{-2\lambda\mu}{\lambda+2\mu}\partial_y & 0 & 0 & 0 & \frac{-\lambda}{\lambda+2\mu} \\ -\mu\partial_y & -\mu\partial_x & 0 & 0 & 0 & 0 \\ 0 & 0 & 0 & -1 & 0 & 0 \end{bmatrix} \tag{8}$$

and

$$\underline{\underline{Q}}_y = \begin{bmatrix} 0 & 0 & 0 & 0 & 0 & 0 \\ 0 & 0 & 0 & 0 & 0 & 0 \\ 0 & 0 & 0 & 0 & 0 & 0 \\ -\mu\partial_y & -\mu\partial_x & 0 & 0 & 0 & 0 \\ -\frac{2\lambda\mu}{\lambda+2\mu}\partial_x & -\zeta\partial_y & 0 & 0 & 0 & \frac{-\lambda}{\lambda+2\mu} \\ 0 & 0 & 0 & 0 & -1 & 0 \end{bmatrix} \tag{9}$$

The interface boundary conditions may then be expressed in the form

$$\underline{\hat{r}}^{(1)}(h) = \underline{\hat{r}}^{(2)}(h) \tag{10}$$

where superscripts indicate the respective media.

Recalling that the goal is to relate the scattered field to the background field (scattered from the mean planar surface), $\underline{r}(h)$ is extrapolated to the mean planar surface by the power series expansion

$$\underline{r}(h) = \underline{r}(0) + h\underline{r}^{(j)}_{,z}(0) + \frac{h^2}{2!}\underline{r}_{,zz}(0) + \ldots \tag{11}$$

Making use of the wave equation (3), (11) is reduced to the form

$$\underline{r}(h) = (\underline{\underline{I}} + h\underline{\underline{A}} + \frac{h^2}{2!}\underline{\underline{A}}^2 + \ldots)\underline{r}(0)\,. \tag{12}$$

So far the formulation is exact as long as the series in (12) converges. It is easy to demonstrate convergence for the case of a planar interface. This series then converges to

$$\underline{r}(h) = e^{h\underline{\underline{A}}}\underline{r}(0)\,. \tag{13}$$

The meaning of $e^{h\underline{\underline{A}}}$ is easily expressed in the (k_x, k_y) Fourier transform domain. For constant h, the transform is done by replacing ∂_x and ∂_y in $\underline{\underline{A}}$ by ik_x and ik_y, respectively, and formally summing the series in (12). The result is the standard form for the propagator matrix (Aki and Richards, 1980, p. 275), which is an exact extrapolation operator and the basis of the propagator matrix method for formulating wave equation solutions in plane layered media (Kennett, 1983). It is clear that a simple form for (12) cannot be obtained when h is allowed to vary.

After the displacement-stress vectors along the rough interface have been extrapolated to the mean planar interface, they are expanded in a perturbation series about $\underline{r}_0(0)$, the displacement-stress vector at the interface of the background planar interface model:

$$\underline{r}^{(j)}(0) = \underline{r}_0(0) + h\underline{r}_1^{(j)}(0) + h^2\underline{r}_2^{(j)}(0) + \ldots \tag{14}$$

Since $\underline{r}_0(0)$ is the displacement-stress vector for the background planar interface model, it is continuous across the boundary and needs no superscript. The higher order terms reflect the influence of the rough interface. Combining (7), (12), and (14), each side of the boundary condition expressed in (10) is written as (omitting the superscripts)

$$\begin{aligned}
\hat{\underline{r}}(h) &= (\underline{\underline{I}} + h_{,x}\underline{\underline{Q}}_x + h_{,y}\underline{\underline{Q}}_y) \\
&\cdot \left(\underline{\underline{I}} + h\underline{\underline{A}} + \frac{h^2}{2!}\underline{\underline{A}}^2 + \ldots\right) \qquad (15) \\
&\cdot (\underline{r}_0 + h\underline{r}_1 + h^2\underline{r}_2 + \ldots) \\
&\approx (\underline{\underline{I}} + h_{,x}\underline{\underline{Q}}_x + h_{,y}\underline{\underline{Q}}_y)\underline{r}_0 + h\underline{\underline{A}}\,\underline{r}_0 + h\underline{r}_1 \qquad (16) \\
&+ O(h^2) + O(hh_{,x}) + O(hh_{,y})
\end{aligned}$$

where $O(\cdot)$ denotes order of accuracy.
Applying the boundary condition (10) to (14) results in

$$\begin{aligned}
h(\underline{r}_1^{(2)} - \underline{r}_1^{(1)}) &= h(\underline{\underline{A}}^{(1)} - \underline{\underline{A}}^{(2)})\underline{r}_0 + h_{,x}(\underline{\underline{Q}}_x^{(1)} - \underline{\underline{Q}}_x^{(2)})\underline{r}_0 \qquad (17) \\
&+ h_{,y}(\underline{\underline{Q}}_y^{(1)} - \underline{\underline{Q}}_y^{(2)})\underline{r}_0 \,.
\end{aligned}$$

The right-hand side of (17) would be zero in a planar interface model. Discontinuities in the displacement-stress vector, such as occurs here, represent sources(Aki and Richards, 1980, p. 38). Thus, the effect of a rough interface is to appear to add sources along the mean planar interface. These sources will be designated by $\underline{s} = h(\underline{r}_1^{(2)} - \underline{r}_1^{(1)})$. This use of sources to represent material deviations from a background model is shared with standard Born theoretical developments. The mapping of heterogeneity into source terms is also used in exact formulations based on Huygen's principle (Paul and Campillo, 1988).
Fourier transforming (17) to the k_x, k_y domain,

$$\underline{s}(k_x, k_y; h = 0) = \frac{1}{4\pi^2}\int_{-\infty}^{\infty} h(k_x - k'_x, k_y - k'_y)\underline{\underline{L}}(k_x, k_y; k'_x, k'_y)\underline{r}_0(k'_x, k'_y)\,dk'_x\,dk'_y \tag{18}$$

where $\underline{\underline{L}}$ is defined by

$$\underline{\underline{L}} = \begin{bmatrix} 0 & 0 & 0 \\ 0 & 0 & 0 \\ ik_x'(\frac{\lambda_1}{\lambda_1+2\mu_1} - \frac{\lambda_2}{\lambda_2+2\mu_2}) & -ik_y'(\frac{\lambda_1}{\lambda_1+2\mu_1} - \frac{\lambda_2}{\lambda_2+2\mu_2}) & 0 \\ k_x k_x'(\zeta_1 - \zeta_2) + k_y k_y'(\mu_1 - \mu_2) - \omega^2(\rho_1 - \rho_2) & 2k_x k_y'(\frac{\lambda_1\mu_1}{\lambda_1+2\mu_1} - \frac{\lambda_2\mu_2}{\lambda_2+2\mu_2}) + k_x' k_y(\mu_1 - \mu_2) & 0 \\ k_x k_y'(\mu_1 - \mu_2) + 2k_x' k_y(\frac{\lambda_1\mu_1}{\lambda_1+2\mu_1} - \frac{\lambda_2\mu_2}{\lambda_2+2\mu_2}) & k_x k_x'(\mu_1 - \mu_2) + k_y k_y'(\zeta_1 - \zeta_2) - \omega^2(\rho_1 - \rho_2) & 0 \\ 0 & 0 & -\omega^2(\rho_1 - \rho_2) \end{bmatrix}$$

$$\begin{bmatrix} \frac{1}{\mu_1} - \frac{1}{\mu_2} & 0 & 0 \\ 0 & \frac{1}{\mu_1} - \frac{1}{\mu_2} & 0 \\ 0 & 0 & \frac{1}{\lambda_1+2\mu_1} - \frac{1}{\lambda_2+2\mu_2} \\ 0 & 0 & -ik_x(\frac{\lambda_1}{\lambda_1+2\mu_1} - \frac{\lambda_2}{\lambda_2+2\mu_2}) \\ 0 & 0 & -ik_y(\frac{\lambda_1}{\lambda_1+2\mu_1} - \frac{\lambda_2}{\lambda_2+2\mu_2}) \\ 0 & 0 & 0 \end{bmatrix} \tag{19}$$

Definition of the Scattering Kernel

The perturbation method developed above will now be used to examine the dominant features of the three-dimensional field scattered from a rough interface. For plane wave sources it is possible to define a factorization of the scattered field into a product of the wavenumber spectrum of the interface and a function that is called the scattering kernel. This scattering kernel is independent of the interface roughness function. For a plane wave source of the form

$$\underline{r}_0(k_x', k_y') = 4\pi^2 \underline{r}_p \delta(k_x' - k_x^p, k_y' - k_y^p), \tag{20}$$

equation (18) reduces to

$$\underline{s}(k_x, k_y) = h(k_x - k_x^p, k_y - k_y^p)\underline{\underline{L}}(k_x, k_y; k_x^p, k_y^p)\underline{r}_0(k_x^p, k_y^p). \tag{21}$$

The scattered field source term in this case is separated into a part associated with a particular interface roughness, $h(k_x - k_x^p, k_y - k_y^p)$, and a part associated with the general scattering properties of the medium, $\underline{\underline{L}}(k_x, k_y; k_x^p, k_y^p)\underline{r}_0(k_x^p, k_y^p)$. The latter part is designated as the scattering kernel. Knowledge of the scattering kernel allows one to evaluate the scattering potential of a material contrast independent of any particular interface.

The transmission scattering kernels for the two-dimensional model in Figure 8 are given in Figure 2. Superimposed on these plots is the Fourier transform of the interface. The scattered field is simply the product of the two curves. From these plots it is clear that a smaller correlation length, and hence a wider Gaussian in the transform domain, would result in large amplitude cusps for large scattering angles in P and S. For the transmitted P wave, the scattered wave amplitude increases for scattering angles larger than the P reflection critical angle. This amplitude boost at large angles may be seen in the P and S reflection coefficients for models D and E in Figures 13(d and e). This effect has also been demonstrated by Levander and Hill (1985) using finite difference methods and by by Paul and Campillo (1988) using boundary integral equation methods.

Describing Reflection and Transmission

The source term given by (18) generates P and S waves above and below the interface. To determine the displacement coefficients of these waves requires a relation between the displacement-stress vector and the up- and down-going P, SV, and SH wave components, the form of which is given by

$$\underline{r} = \underline{\underline{F}}\,\underline{b} \; . \tag{22}$$

where $\underline{b} = [\grave{P}\ \grave{S}\ \grave{T}\ \acute{P}\ \acute{S}\ \acute{T}]^T$, $\grave{}$ and $\acute{}$ denote down- and up-going waves, respectively, and P, S, and T are the displacement coefficients of P, SV, and SH waves, respectively. Using the reflection coefficient sign conventions of Aki and Richards (1980), $\underline{\underline{F}}$ is given by

$$\underline{\underline{F}} = \begin{bmatrix} \frac{k_x\alpha}{\omega} & \frac{k_x\nu\beta}{\omega K} & -\frac{k_y}{K} & \frac{k_x\alpha}{\omega} & \frac{k_x\nu\beta}{\omega K} & -\frac{k_y}{K} \\ \frac{k_y\alpha}{\omega} & \frac{k_y\nu\beta}{\omega K} & \frac{k_x}{K} & \frac{k_y\alpha}{\omega} & \frac{k_y\nu\beta}{\omega K} & \frac{k_x}{K} \\ \frac{\gamma\alpha}{\omega} & -\frac{K\beta}{\omega} & 0 & -\frac{\gamma\alpha}{\omega} & \frac{K\beta}{\omega} & 0 \\ \frac{2ik_x\gamma\alpha\mu}{\omega} & \frac{ik_x(\nu^2-K^2)\beta\mu}{\omega K} & -\frac{ik_y\nu\mu}{K} & -\frac{2ik_x\gamma\alpha\mu}{\omega} & -\frac{ik_x(\nu^2-K^2)\beta\mu}{\omega K} & \frac{ik_y\nu\mu}{K} \\ \frac{2ik_y\gamma\alpha\mu}{\omega} & \frac{ik_y(\nu^2-K^2)\beta\mu}{\omega K} & \frac{ik_x\nu\mu}{K} & -\frac{2ik_y\gamma\alpha\mu}{\omega} & -\frac{ik_y(\nu^2-K^2)\beta\mu}{\omega K} & -\frac{ik_x\nu\mu}{K} \\ \frac{i(\nu^2-K^2)\alpha\mu}{\omega} & -\frac{2iK\nu\beta\mu}{\omega} & 0 & \frac{i(\nu^2-K^2)\alpha\mu}{\omega} & -\frac{2iK\nu\beta\mu}{\omega} & 0 \end{bmatrix}$$

$$\bullet \begin{bmatrix} e^{i\gamma z} & 0 & 0 & 0 & 0 & 0 \\ 0 & e^{i\nu z} & 0 & 0 & 0 & 0 \\ 0 & 0 & e^{i\nu z} & 0 & 0 & 0 \\ 0 & 0 & 0 & e^{-i\gamma z} & 0 & 0 \\ 0 & 0 & 0 & 0 & e^{-i\nu z} & 0 \\ 0 & 0 & 0 & 0 & 0 & e^{-i\nu z} \end{bmatrix} \tag{23}$$

with $K = \sqrt{k_x^2 + k_y^2}$, $\gamma = \sqrt{\omega^2/\alpha^2 - K^2}$, and $\nu = \sqrt{\omega^2/\beta^2 - K^2}$. To recover scattered field displacements from the source term note that

$$\underline{s} = \underline{r}^{(2)} - \underline{r}^{(1)} = \underline{\underline{F}}^{(2)}\underline{b}^{(2)} - \underline{\underline{F}}^{(1)}\underline{b}^{(1)} \tag{24}$$

and that $\underline{s}$ generates no down-going waves in the upper medium and no up-going waves in the lower medium. Hence,

$$\underline{s} = \begin{bmatrix} F_{11}^{(2)} & F_{12}^{(2)} & F_{13}^{(2)} & -F_{14}^{(1)} & -F_{15}^{(1)} & -F_{16}^{(1)} \\ F_{21}^{(2)} & F_{22}^{(2)} & F_{23}^{(2)} & -F_{24}^{(1)} & -F_{25}^{(1)} & -F_{26}^{(1)} \\ F_{31}^{(2)} & F_{32}^{(2)} & F_{33}^{(2)} & -F_{34}^{(1)} & -F_{35}^{(1)} & -F_{36}^{(1)} \\ F_{41}^{(2)} & F_{42}^{(2)} & F_{43}^{(2)} & -F_{44}^{(1)} & -F_{45}^{(1)} & -F_{46}^{(1)} \\ F_{51}^{(2)} & F_{52}^{(2)} & F_{53}^{(2)} & -F_{54}^{(1)} & -F_{55}^{(1)} & -F_{56}^{(1)} \\ F_{61}^{(2)} & F_{62}^{(2)} & F_{63}^{(2)} & -F_{64}^{(1)} & -F_{65}^{(1)} & -F_{66}^{(1)} \end{bmatrix} \begin{bmatrix} \dot{P}^{(2)} \\ \dot{S}^{(2)} \\ \dot{T}^{(2)} \\ \dot{P}^{(1)} \\ \dot{S}^{(1)} \\ \dot{T}^{(1)} \end{bmatrix} \tag{25}$$

$$= \underline{\underline{\hat{F}}}\,\underline{\hat{b}}$$

The wave displacement coefficients generated by $\underline{s}$ are given by

$$\hat{\underline{b}} = \hat{\underline{\underline{F}}}^{-1} \underline{s} \tag{26}$$

The inverse of $\hat{\underline{\underline{F}}}$ exists for all values of (k_x, k_y) except $(k_x, k_y) = (0,0)$. At this point in the $\underline{k}$ plane the scattered waves are propagating normal to the mean planar surface, and SV waves are indistinguishable from SH waves. For example, consider an S plane wave traveling in the z direction with particle motion in the x direction. If the wave direction is slightly perturbed in the x direction it becomes an SV wave. A perturbation in the y direction makes it an SH wave. These distinctions are true even when the perturbations are infinitesimal. Hence, to remove the singularity of $\hat{\underline{\underline{F}}}$, an arbitrary naming convention must be adopted for vertically propagating S waves. In this paper, the x component of such waves is labeled SV, and the y component is labeled SH. The $\hat{\underline{\underline{F}}}$ matrix for vertical propagation is

$$\underline{\underline{F}}(0,0) = \begin{bmatrix} 0 & 1 & 0 & 0 & -1 & 0 \\ 0 & 0 & 1 & 0 & 0 & -1 \\ 1 & 0 & 0 & 1 & 0 & 0 \\ 0 & i\omega\rho_2\beta_2 & 0 & 0 & i\omega\rho_1\beta_1 & 0 \\ 0 & 0 & i\omega\rho_2\beta_2 & 0 & 0 & i\omega\rho_1\beta_1 \\ i\omega\rho_2\alpha_2 & 0 & 0 & -i\omega\rho_1\alpha_1 & 0 & 0 \end{bmatrix} \tag{27}$$

COMPARISON WITH FINITE DIFFERENCE

The simple form of the scattered field source term (18) was made possible by the truncation of (15) to yield a low order perturbation approximation (16). The error resulting from the exclusion of higher order terms is difficult to evaluate analytically. It is possible, though, to determine bounds on the domain of validity of this approximation. Kennett (1972) derived two conditions on the model which must hold in order for(18) to be valid. The first condition constrains the scattered field to be much weaker than the background field, a requirement for the single scattering approximation to apply. This condition is expressed by the relation

$$\underline{s}(k_x, k_y; h = 0) \ll \max_{k_x, k_y} |\underline{r}_0(k_x, k_y)|, \tag{28}$$

where $\underline{s}$ is the scattered field source term defined by (18). Kennett (1972) reduced this to a simpler, but stricter, form by replacing the convolution integral in (18) by an upper-bound approximation, yielding

$$\frac{\kappa_0 \omega L}{\pi \beta_1} \eta_{12} \max_x |h(x)| \ll 1, \qquad \max_x |h_{,x}(x)| \ll 1, \tag{29}$$

where

$$\eta_{12} = \max \left\{ \left| \frac{\alpha_1 \rho_1 - \alpha_2 \rho_2}{\alpha_1 \rho_1 + \alpha_2 \rho_2} \right|, \left| \frac{\beta_1 \rho_1 - \beta_2 \rho_2}{\beta_1 \rho_1 + \beta_2 \rho_2} \right| \right\},$$

L is the periodicity length of the rough interface, and the wavenumber spectrum of the incident field is bounded by $|k| \leq \kappa_0$. The second condition is that the background field must not contain wavenumbers so close to grazing incidence that shadow zones form. Shadow zones will be avoided if the radius of curvature of the interface is much longer than a wavelength. Such waves will then propagate as guided waves along the interface. This condition is expressed by

$$\frac{1}{\sqrt{\kappa_0^2 + k_z^2}} \max_x |h_{,xx}| \ll 1, \tag{30}$$

where k_z is the vertical wavenumber component associated with the maximum horizontal component κ_0.

These conditions are not satisfactory for practical use, however. Approximations used in the derivation of (29) result in a much stricter bound than is necessary, and the practical limit imposed by(30) needs to be better defined. In order to empirically construct more realistic constraints on interface roughness, reflection and transmission coefficients obtained using the perturbation method described above will be compared to those derived from two-dimensional finite difference solutions. By comparing results for a range of interface height and slope statistics, using a normal incidence plane wave source, the domain of validity of the perturbation method can be explored. Three-dimensional model comparisons using the finite difference method were not possible with the computational resources available for this study. The similarity of the two- and three-dimensional perturbation formulations allows the results of the two-dimensional validity check to be applied to three-dimensional models.

The finite difference algorithm used here is a two-dimensional second-order formulation. To summarize, the wave equations (1) and (2) are solved in the time-space domain by replacing the time and space derivatives by their second-order centered-difference approximations. The accuracy is improved by using a staggered mesh formulation in which horizontal and vertical displacements are represented on separate grids, each shifted by half of the grid point spacing in both coordinate directions with respect to the other. This has the added benefit of increasing the grid-point density by a factor of two. The formulation differs from that of Virieux (1986) in that we use the second-order displacement/stress wave equations instead o the first-order velocity/stress equations. This modification improves efficiency, since the final solution was desired in terms of displacement. The stability conditions and

grid dispersion relations are identical with those of Virieux's formulation. A low-order, staggered-mesh scheme was chosen because it is the most efficient method when dense grid point spacings are necessary, as is the case in our models where small interface irregularities must be represented. Higher order schemes, such as those which use fourth-order (Bayliss, *et al.*) or Fourier spatial derivative operators (Kosloff *et al.*, 1984; Fornberg, 1988), are generally thought to be more efficient than second-order schemes, but this is not necessarily true. The dense grid point spacing used in modeling small interface perturbations puts the second-order derivative operator well within its domain of acceptable accuracy, and the short operator length makes it the most efficient scheme.

The finite difference method is known to be accurate when the wave fields and the model are both well discretized. Hence, when models with large interface irregularities are compared, the finite difference method will be used as the standard. On the other hand, the perturbation method is accurate for models with small interface height and slope irregularities and will be used as the standard for such models. The comparison with finite difference solutions will proceed in two parts. First it is necessary to show that the range of interface irregularities over which the finite difference method is accurate extends into the range over which the perturbation method is accurate. This will be done by showing that the finite difference method results match the perturbation method results for a model with very small height and slope irregularities. If the finite difference method works well in this case, results for larger interface irregularities will also be valid because they will be more accurately represented on the finite difference grid. Finite difference solutions will then be used a basis for comparison with perturbation solutions for a series of models with larger height and slope irregularities in order to probe the limits of validity of the perturbation approximation.

Accuracy of the Finite Difference Method

All results for scattering from a rough interface in this paper are expressed as reflection and transmission coefficients. The procedure for deriving these coefficients from the finite difference solution is similar to that described in Section for the perturbation solution. In short, equation (22) is used to convert $\underline{r}$ into $\underline{b}$, and then P and S wave amplitudes in $\underline{b}$ are scaled by the source wave amplitude. The displacements and stresses in $\underline{r}$ are computed by the finite difference method in the time-space domain along a horizontal linear array of uniformly spaced receivers that do not intersect the interface at any point. The receiver array should be between the source and the interface in order to separate incident waves from reflected waves. $\underline{r}$ is then Fourier transformed into the ω-k domain to yield a form suitable for use in (22). The distance of the receiver array from the interface is accounted for by the z term in the definition of $\underline{\underline{E}}$ in equation (23). If the finite difference model is such that reflections from the edge of the grid will arrive within the seismogram time window,

absorbing boundaries must be implemented with attenuate these reflections to a level much smaller than the reflection and transmission coefficients to be measured. The length of the array, L, controls the wavenumber sampling increment, $\Delta k = 2\pi/L$, and should be set to the horizontal dimension of the finite difference grid to avoid aliasing. From here forward L is taken to be equal to the horizontal dimension of the grid. For a point source, L controls the range of incidence and scattering angles that are within the receiver array, and the horizontal grid size should be large enough to capture the incidence and scattering angles of interest. Since the range of incident and scattering angles detected is also dependent on the distance of the source and the array from the interface, it is best to put the source and the receiver array as close to the interface as possible in order to minimize the grid size and the seismogram length. The spacing of the receivers controls the maximum representable wavenumber in $\underline{r}$, and should be set equal to the grid spacing to avoid aliasing.

The reflection and transmission coefficients obtained from finite difference modeling are be compared with analytical coefficients in the case of a planar interface model. The model is shown in Figure 3. The source has an 18 Hz Ricker time function of the form

$$R(t) = (1 - \frac{1}{2}\omega_0^2 t^2) e^{-\frac{1}{4}\omega_0^2 t^2}, \tag{31}$$

where ω_0 is the primary angular frequency of the wavelet. The source is implemented as a *body force term of the form*

$$\underline{f} = R(t) \begin{bmatrix} -(x - x_s) e^{-(x-x_s)^2/2} \\ -(z - z_s) e^{-(z-z_s)^2/2} \end{bmatrix}, \tag{32}$$

representing an explosion source smoothed by a Gaussian with standard deviation equal to the grid point spacing. This smoothing is necessary to make the explosion dipoles, which contain energy at infinite wavenumbers, representable on the finite difference grid. The source isotropically radiates pure P waves. It is located 20 grid points above the interface, and the two arrays of receivers are located 10 grid points above and 10 grid points below the interface. Reflection and transmission coefficients derived from the finite difference seismograms for this model are shown in Figure 4 along with analytical coefficients. There is generally good agreement for both pre- and post-critical waves. The small disagreement present at the larger scattering angles results from the finite aperture of the receiver array.

Another check on the accuracy of the reflection and transmission coefficient results is to plot the coefficients for the non-physical waves in the solution: the down-going S in the upper medium and the up-going S and P in the lower medium. These coefficients are shown in Figure 5. For each wavenumber, the coefficients are normalized by the amplitude of the down-going P wave source. Hence, the down-going P wave coefficient has unit amplitude for all angles. The remaining three coefficients plotted here are indicative of error in the

conversion of the measured finite difference displacements and stresses into wave coefficients. In general, the amplitude of the non-physical waves increases with increasing scattering angle, since the wavenumbers corresponding to these larger angles are less well represented by the receiver array.

The effect of changing the array aperture is illustrated by the results of another finite difference model which is identical to the previous model (Figure 3) except that the grid dimensions and receiver array sizes are doubled. The spacing between receivers in each array is unchanged. A comparison of reflection and transmission coefficients derived from this model with analytical results is shown in Figure 6. The non-physical coefficients for this model are shown in Figure 7. The ringing observed in Figure 4 is amplified. In addition, the seismogram time window in this model was inadvertently set large enough to allow the upward-traveling source wave to reach the top of the grid and wrap around to the bottom of the grid (we are using periodic boundary conditions) to intersect the lower receiver array. This results in the large lower medium up-going P wave coefficient shown in Figure 7 at small scattering angles, and to a lesser extent affects the accuracy of the lower medium down-going P wave coefficient shown in Figure 6.

The finite difference and perturbation methods will now be compared for a model with very small height and slope perturbations shown in Figure 8. The source is a downward propagating, planar P wave with an 18 Hz Ricker time function. The interface roughness has a Gaussian autocorrelation function with a correlation length of $L = 100$ m and an rms height deviation of $\sigma = 16.7$ m. The interface is periodic with a period of 2.70 km, the width of the model. The Fourier transform of the interface function which has been discretized for the finite difference grid is shown in Figure 9a as a function of horizontal slowness evaluated at 18 Hz. The value is set to zero at the origin in order to have zero mean interface deviation. It would be a perfect Gaussian were it not for the finite difference discretization. Histograms of interface height and slope are shown in Figures 9b and 9c. The largest deviation from the mean planar surface is 12 m, or 15 percent of the S wavelength in the upper medium. The largest slope is 0.16, while the mean and standard deviation of the slope are zero and 0.059, respectively. Since the maximum interface height and slope are fairly well approximated by twice their standard deviations, histograms will not be provided for the remaining rough interfaces used in this study. A comparison of the reflection and transmission coefficients derived from the finite difference and perturbation methods is shown in Figure 10. Agreement is very good, with both amplitude and shape predicted well by the perturbation method. "Ringing" appears to some degree on all of the finite difference coefficient plots, and is most apparent on the S wave coefficient plots. Plots of the non-physical coefficients for the finite difference data are shown in Figure 11. The down-going P wave in the upper medium has unit amplitude at zero angle. It is clear from this figure that the maximum error is less than 0.1 percent, and that this error is associated with the S wave in the upper medium.

This error is enough to explain the difference between the finite difference and perturbation results for the reflected S wave coefficient at large scattering angles.

Domain of Validity for the Perturbation Method

The domain of validity of the perturbation method will be explored by comparing reflection and transmission coefficients generated using the perturbation method with those derived from finite difference modeling. Six rough interface models are used in this comparison, each having a Gaussian autocorrelation function and a uniform random phase. The interface functions are shown in Figure 12(a–f) with two times vertical exaggeration. RMS interface slope ranges from 0.037 to 0.99 and RMS interface height is 0.01 km for models A–E and 0.015 Km for model F. Since the accuracy of the perturbation method is sensitive to the smallest elastic wavelength in the model, interface height is measured here in terms of S wavelengths in the upper medium (S_1), and thus the relative height of the irregularities changes as the frequency changes. The bandwidth of the 18 Hz Ricker wavelet time function used in the finite difference calculation allowed reflection and transmission coefficients to be computed at three frequencies (9.93, 16.5, and 26.5 Hz) in each of the six models, for a total of 18 comparisons for each coefficient. In these comparisons, RMS interface height ranges from 0.069 to 0.28 S_1 wavelengths. RMS height, correlation length, and RMS slope for the models used are listed in Table 1. The material parameters are $\alpha_1 = 2.50$ km/s, $\beta_1 = 1.44$ km/s, $\rho_1 = 1.00$ g/cm^3, $\alpha_2 = 3.00$ km/s, $\beta_2 = 1.73$ km/s, and $\rho_2 = 1.00$ g/cm^3. The source is a normally incident planar P wave in layer one. These comparisons are shown for models A–F in Figures 13(a–f). The reflection and transmission coefficients are the displacement coefficients $\acute{P}_1$, $\acute{S}_1$, $\grave{P}_2$, and $\grave{S}_2$ are normalized so that $\grave{P}_1 = 1$.

In order to facilitate the comparison of the perturbation and finite difference coefficients, the curves are compared by finding the L_2 norm difference defined by

$$\|C_{pt} - C_{fd}\|_2 = 100 \times \frac{\int_0^{\frac{\pi}{2}} [\acute{P}_{pt}(\theta_s) - \acute{P}_{fd}(\theta_s)]^2 d\theta_s}{\int_0^{\frac{\pi}{2}} \acute{P}_{fd}(\theta_s)^2 d\theta_s} \tag{33}$$

where θ_s is the scattering angle and the $\acute{P}$ coefficient is chosen for illustration. The differences between method results are plotted for each of the four coefficients in Figures 14(a–d) for constant RMS interface height, and in Figures 14(e–h) for constant RMS interface slope. The constant height plots show that the accuracy of the perturbation solution is not significantly degraded as RMS interface slope varies within the range tested. This L_2 norm result is verified in the coefficient comparison plots in Figures 13(a–f). The constant slope plots show that error increases rapidly with increasing RMS interface height, and in this particular example is acceptable for values of RMS height less than about 0.1 S_1 wavelengths.

FEATURES OF THE 3-D SCATTERED FIELD

Three-dimensional scattering examples will now be presented for the model shown in Figure 15. The material and interface parameters are identical to those of model D (see Table 1 and Figure 12) with the Gaussian auto-correlation function having identical correlation lengths in the x and y directions. In general, a Gaussian rough interface whose major and minor axes coincide with the x and y axes has a Gaussian auto-correlation function of the form

$$h(k_x, k_y)h^*(k_x, k_y) \sim e^{-\frac{(k_x L_x)^2 + (k_y L_y)^2}{2}}. \tag{34}$$

where L_x and L_y are the major- and minor-axis correlation lengths. Equation (34) can be generalized to allow roughness trends at an angle θ to the x axis by applying a rotation transformation to get

$$h(k_x, k_y)h^*(k_x, k_y) \sim e^{-\frac{1}{2}\left[L_x^2(k_x\cos(\theta)+k_y\sin(\theta))^2 + L_y^2(-k_x\sin(\theta)+k_y\cos(\theta))^2\right]}. \tag{35}$$

In the first example, the source is an 18 Hz planar SV wave propagating downward along the z axis with particle motion in the x direction. The SV wave scatters into reflected and transmitted P, SV, and SH waves. The three-dimensional P, SV, and SH transmission coefficients for this model, found using the perturbation method, are given in Figure 16. The x and y scattering angles in these figures, referred to as ϕ_x and ϕ_y in the text, are measured from the downward z axis in the x-z and y-z planes, respectively. They are defined by $\phi_x = \sin^{-1}(k_x v/\omega)$ and $\phi_y = \sin^{-1}(k_y v/\omega)$ where v is the body wave velocity of the transmitted wave concerned. Scattering in the z-direction, for example, is given by $\phi_x = \phi_y = 0$. The transmission coefficient plots cover scattering angles in the range $-90° \leq \phi_x \leq 90°$ and $0° \leq \phi_y \leq 90°$, and are symmetric about the $\phi_y = 0$ axis. For all three scattered wavetypes, these plots show that scattering is maximal in the direction that conserves source particle motion: for an SV source, P and SV are maximally scattered in the x-z plane ($\phi_y = 0$), and SH is maximally scattered in the y-z plane ($\phi_x = 0$). This effect is exaggerated by the use of the single scattering approximation. A null is present in the plane normal to maximal plane: the y-z plane for P and SV waves and the x-z plane for SH waves. An alternative display of the three-dimensional transmission coefficients is a cross-section of the coefficients for all scattering angles at a particular azimuth, where azimuth is measured clockwise in the x-y plane from the x-axis, and the scattering angle is defined by $\psi = \sin^{-1}(Kv/\omega)$. Cross-sections of the reflection and transmission coefficients for the same model and source parameters are given for azimuthal angles of 10°, 45°, and 80°in Figure 17.

Transmission scattering kernels for the model in Figure 15 are given in Figure 18. Comparison with the SV and SH transmission coefficients in Figure 16 shows that the spatially band-limited nature of this particular interface damps out the large amplitude features

present at large scattering angles. The P transmission coefficient exhibits a hint of the cusps present in the kernel. Consideration of another interface roughness function requires only a visual superposition of the new interface spectrum with the kernel. For the same SV source as above and a two-dimensional rough interface with variation in the x direction, the problem is truly two-dimensional, and waves are scattered into P and SV. If the interface is rotated 90 degrees so that variation is in the y direction, the problem is fully three-dimensional, and waves are scattered into P and SH. More general interfaces whose auto-correlation functions are described by (35), or perhaps a von Karman or exponential function, are handled with the same approach.

The second example is the same as the first, but with the SV source replaced by a P source. The three-dimensional P and SV transmission coefficients for this model are given in Figure 19. Since the source particle motion and the Gaussian auto-correlation function are azimuthally invariant, the scattering coefficients are also azimuthally invariant. Deviations of the contours from circular arcs are artifacts of the contouring program. Reflection and transmission coefficient cross-sections for this model are given in Figure 20. Note that scattered SH waves are not generated in this example. This is a consequence of the single-scattering approximation. For a normal incidence planar P wave, a minimum of two bounces are required to generate SH.

DISCUSSION AND CONCLUSIONS

A perturbation method has been presented here for computing three-dimensional body wave scattering from a rough interface. Its speed and simplicity are such that each of the examples in this paper was generated on a Macintosh SE computer in less than two minutes. Speed is an important consideration when three-dimensional modeling is necessary. For example, many of the two-dimensional finite difference computations done for comparison required 15 Mbytes of core and 23 hours of CPU time on a Vax 8800. In three dimensions, finite difference solutions for these models would be beyond our resources. For the class of irregular interface models with small RMS height deviations, the perturbation method is a useful alternative.

Since interface height deviations in the models presented here are small, comparisons of the perturbation method with the finite difference method were preceded by careful testing of the finite difference method to show that it is valid for the small deviations used in these comparisons. It can be shown that in the limit as the finite difference grid sampling interval goes to zero, and as the numerical precision of the computer goes to infinity, the finite difference solution converges to the exact solution as $O(\Delta x)$ (Brown, 1984). However, in order for the grid sampling interval to be small enough that the finite difference solution is sufficiently close to the exact solution, the number of grid points describing a fixed model must increase as the size of the interface height perturbations decreases. Therefore, the core

size and speed of a computer are constraints in the minimum interface height perturbation that can be accurately modeled using finite difference method. Of course, a planar boundary is an exception to this limit. Another lower limit on interface perturbation size is imposed by numerical precision. As the size of interface height perturbations decreases, the amplitude of scattered seismic waves decreases. Since these scattered waves are added to the relatively large planar interface response, insignificant numerical noise in the planar interface response can be significant when compared with the scattered field. This is probably the cause of the "ringing" present in the finite difference-derived scattering coefficients. Comparisons of finite difference-derived scattering coefficients for a planar model against an analytical solution, and for a model with small interface height and slope perturbations against a perturbation method solution, show that this "ringing" tends to oscillate about the exact solution. Hence, the smoothed finite difference scattering coefficients are useful for comparisons.

Numerous two-dimensional model comparisons of finite difference and perturbation method scattering coefficients are given in Figures 13(a-f). In order to make it easier to spot trends in these comparisons, each comparison is summarized by a single number, the L_2 norm of the difference, which is plotted versus RMS slope for a constant RMS height, and against RMS height for a constant RMS slope, in Figure 14. There are two major trends in the L_2 norm results. The error increases strongly with increasing RMS height, and has acceptable levels for RMS heights of less than about 0.1 S_1 wavelengths. Also, error appears to be roughly constant for increasing RMS slope for the tested range of from 0.037 to 0.99. Smaller trends, such as the apparent increase in accuracy with increasing RMS slope, are misleading. The L_2 norm is overly sensitive to the noise in the finite difference solution being used as the standard for comparison. This is apparent when the scattering coefficient plots in Figures 13(a-f) are examined for the trend seen in the L_2 norm plots. The L_1 norm was also calculated to see whether it is less sensitive to this noise, but the improvements were minimal. Ultimately, all trends must be confirmed by the scattering coefficient plots.

The perturbation method was used to calculate P, SV, and SH scattering for an SV wave normally incident on a three-dimensional rough interface. It was shown that P and SV waves scattering in the azimuth of the incident SV particle motion have maximum amplitude, and that no P or SV waves are scattered in the azimuth normal to the maximal direction. Scattered SH waves have the opposite behavior, scattering maximally in the azimuth normal to the incident SV particle motion. A scattering kernel was defined and demonstrated which allows the scattering radiation pattern to be separated into a part controlled by the material contrast at the interface and a part due to the interface. The scattering kernel for the three-dimensional scattering example shows that scattered wave amplitudes tend to increase in amplitude for scattering angles beyond the P wave critical angle for the background planar interface model.

In the three-dimensional scattering example it was shown that there is a null in P and

SV scattering in the y direction, and a null in SH scattering in the x direction. These nulls do not exist in the time-space domain, where a receiver in any location can detect waves traveling in all directions. Future work includes an extension of the perturbation results to the time-space domain using the discrete wavenumber method (Bouchon, 1977) in order to account for these interference effects.

References

Aki, K., P.G.Richards, 1980, *Quantitative Seismology: Theory and Methods*, W. H. Freeman and Company, San Francisco, vols. 1 and 2, 932 pp.

Bayliss, A., K. Jordan, J. LeMesurier, and E. Turkel, 1986, A fourth-order accurate finite difference scheme for the computation of elastic waves, *Bull. Seism. Soc. Am., 76,* 1115 1132.

Bouchon, M., 1977, Discrete wavenumber representation of seismic-source wave fields, *Bull. Seism. Soc. Am., 67,* 259–277.

Brown, D.L., 1984, A note on the numerical solution of the wave equation with piecewise smooth coefficients, *Math. Comp., 42,* 369 -391.

Caravana, C., S.S. Stubeda, and R. Turpening, 1988, Nine-component zero offset VSP, in Reservoir Delineation—Vertical Seismic Profiling Consortium Annual Report, Earth Resources Laboratory, Department of Earth, Atmospheric, and Planetary Sciences, Massachusetts Institute of Technology, Cambridge, MA, 10-1 10-22.

DeSanto, J.A., and G.S. Brown, 1986, Analytical techniques for multiple scattering from rough surfaces, in *Progress in Optics, XXIII,* E. Wolf (ed.), Elsevier Science Publishers B.V.

Fornberg, B., 1988, The pseudospectral method: Accurate representation of interfaces in elastic wave calculations, *Geophysics, 53,* 625–637.

Gilbert, F., and L. Knopoff, 1960, Seismic scattering from topographic irregularities, *J. Geophys. Res., 65,* 3437–3444.

Hudson, J.A., 1967, Scattered surface waves from a surface obstacle, *Geophys. J. R. astr. Soc., 13,* 441-458.

Kennett, B.L.N., 1972, Seismic wave scattering by obstacles on interfaces, *Geophys. J. R. astr. Soc., 28,* 249–266.

Kennett, B.L.N., 1983, *Seismic Wave Propagation in Stratified Media*, Cambridge University Press, New York, 339.

Kosloff, D., M. Reshef, and D. Loewenthal, 1984, Elastic wave calculations by the Fourier method, *Bull. Seism. Soc. Am.*, *74*, 875–891.

Levander, A.R., and N.R. Hill, 1985, P-SV resonances in irregular low-velocity surface layers, *Bull. Seism. Soc. Am.*, *75*, 847–864.

Paul, A., and M. Campillo, 1988, Diffraction and conversion of elastic waves at a corrugated interface, *Geophysics*, *53*, 1415–1424.

Prange, M., 1987, Efficiency considerations from finite difference elastic wave modeling on the Connection Machine, in *Reservoir Delineation Vertical Seismic Profiling Consortium Annual Report*, Earth Resources Laboratory, Department of Earth, Atmospheric, and Planetary Sciences, Massachusetts Institute of Technology, Cambridge, Mass.

Virieux, J., 1986, P-SV wave propagation in heterogeneous media: velocity-stress finite-difference method, *Geophysics*, *51*, 889–901.

Model	Correlation Length	RMS Slope	RMS Height in S_1 Wavelengths at 9.93 Hz	RMS Height in S_1 Wavelengths at 16.5 Hz	RMS Height in S_1 Wavelengths at 26.5 Hz
A	0.30	0.037	0.069	0.11	0.18
B	0.10	0.10	0.069	0.11	0.18
C	0.050	0.20	0.069	0.11	0.18
D	0.033	0.30	0.069	0.11	0.18
E	0.010	0.99	0.069	0.11	0.18
F	0.15	0.10	0.10	0.17	0.28

Table 1: Interface parameters for the rough interfaces shown in Figure 12.

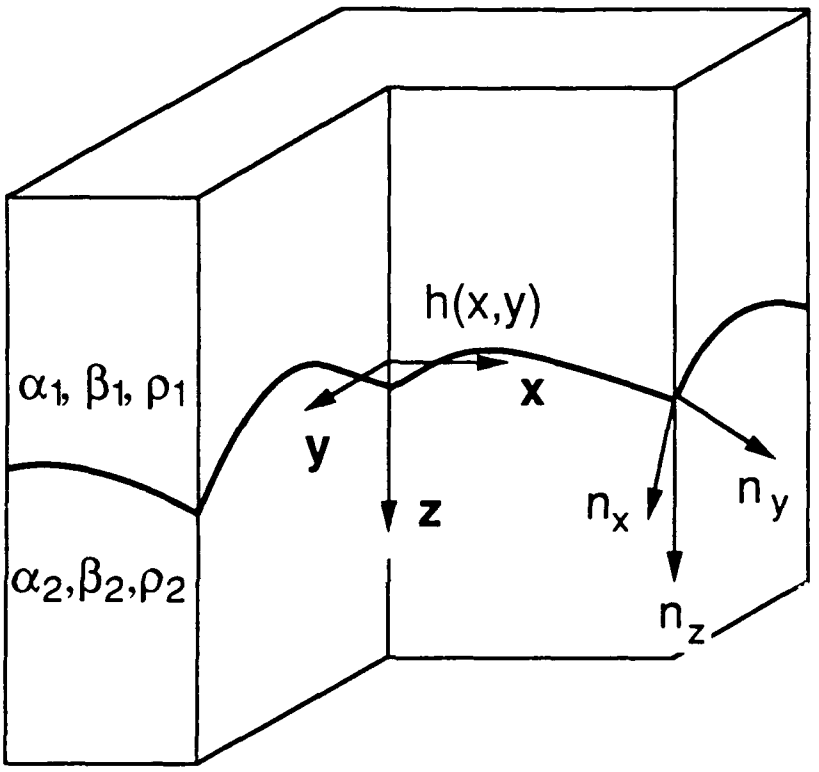

Figure 1: Geometry of the rough interface model. The interface is defined by $z = h$ and the downward-pointing unit normal to this surface is denoted by $\underline{n}$. The $z = 0$ plane is defined as the mean planar surface for the rough interface.

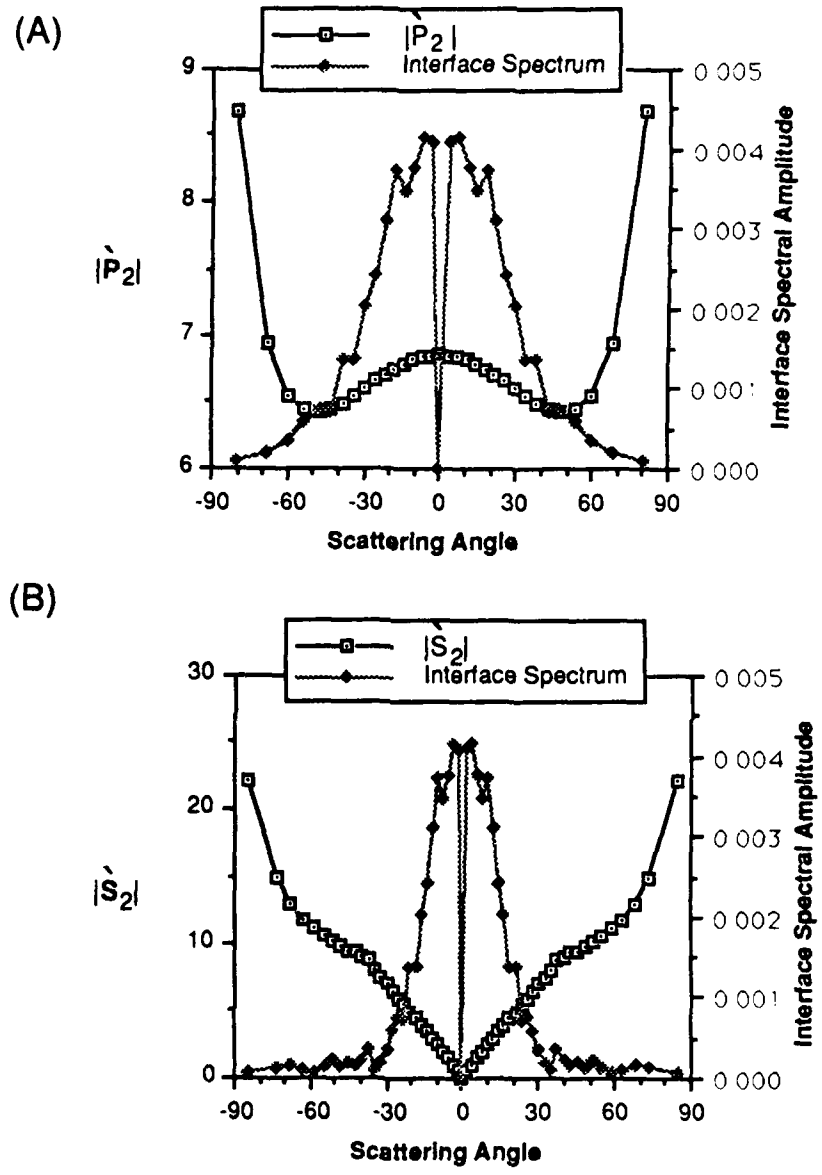

Figure 2: Transmission scattering kernels for the model in Figure 8. The Fourier transform of the interface is superimposed.

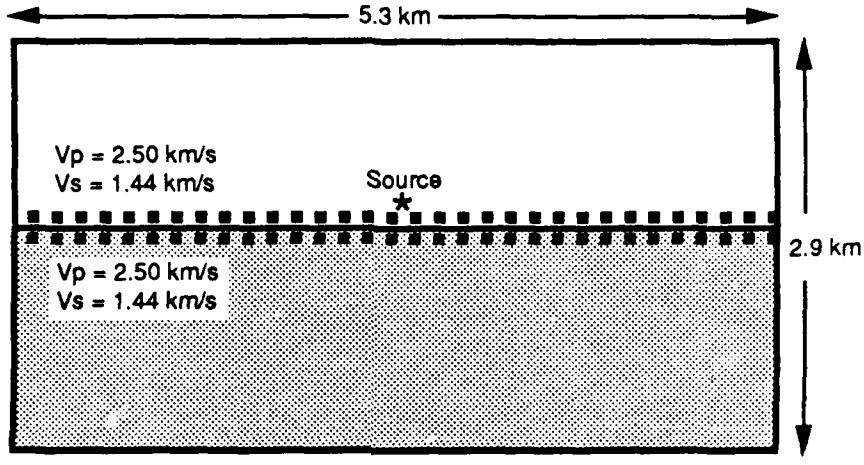

Figure 3: Planar interface model used to compare finite difference derived reflection and transmission coefficients with analytical solutions. The source is a point explosion with an 18 Hz Ricker wavelet time function. The sampling parameters, $\Delta x = \Delta z = 6.67$ m and $\Delta t = 0.00156$ s, result in a maximum phase dispersion error of -1.1 percent at 18 Hz. The source is located 20 grid points above the interface, and the receiver arrays are located 10 grid points on either side of the interface. The horizontal receiver interval is two grid points. All waves within the seismogram time window are contained within the finite difference grid, eliminating the need for absorbing boundaries.

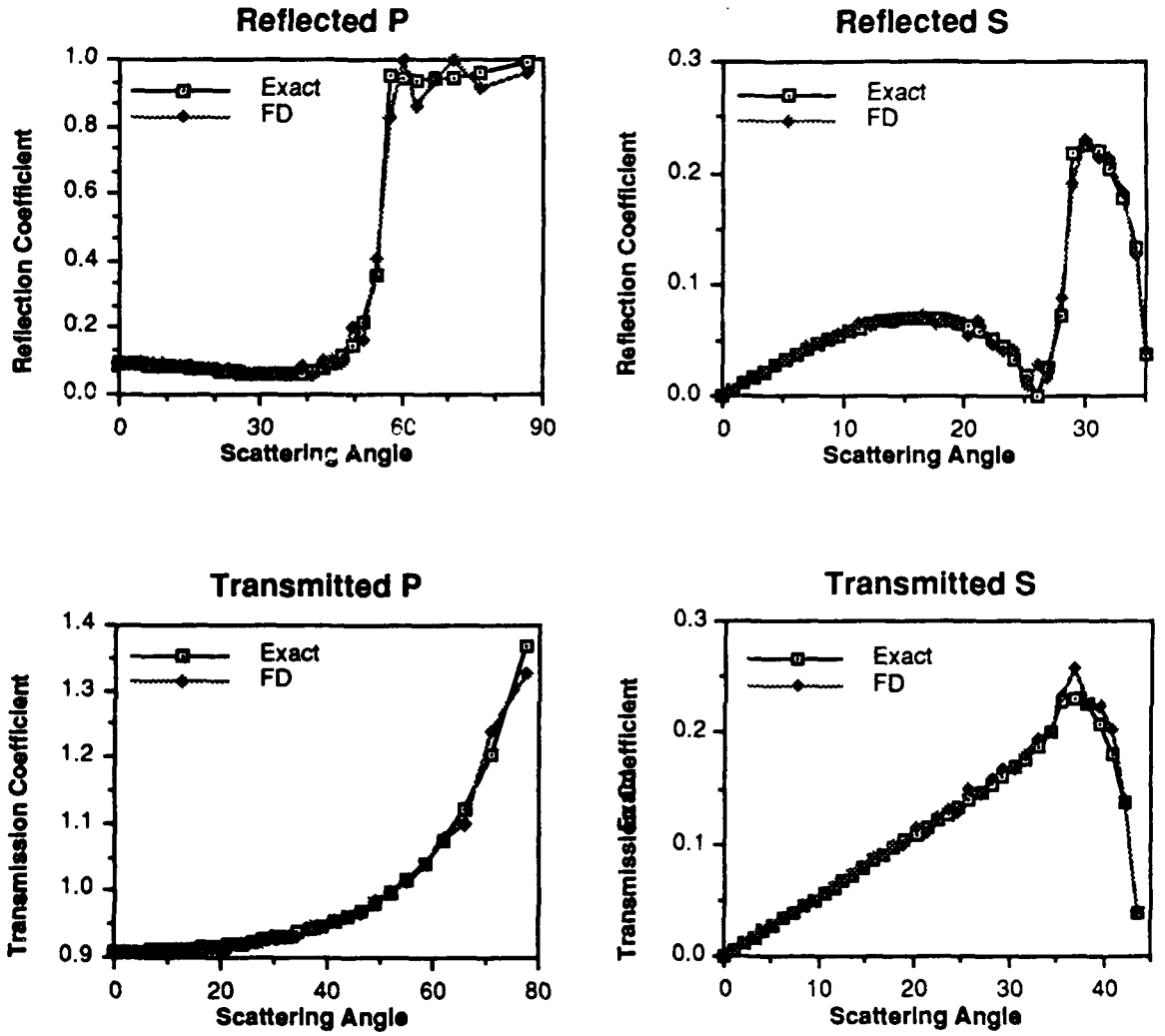

Figure 4: Comparison between P and S wave reflection and transmission coefficients generated by finite difference and analytic methods for a planar interface. The model is shown in Figure 3. The small disagreement present at the larger scattering angles is "Gibb's ringing" that results from the finite aperture of the receiver array.

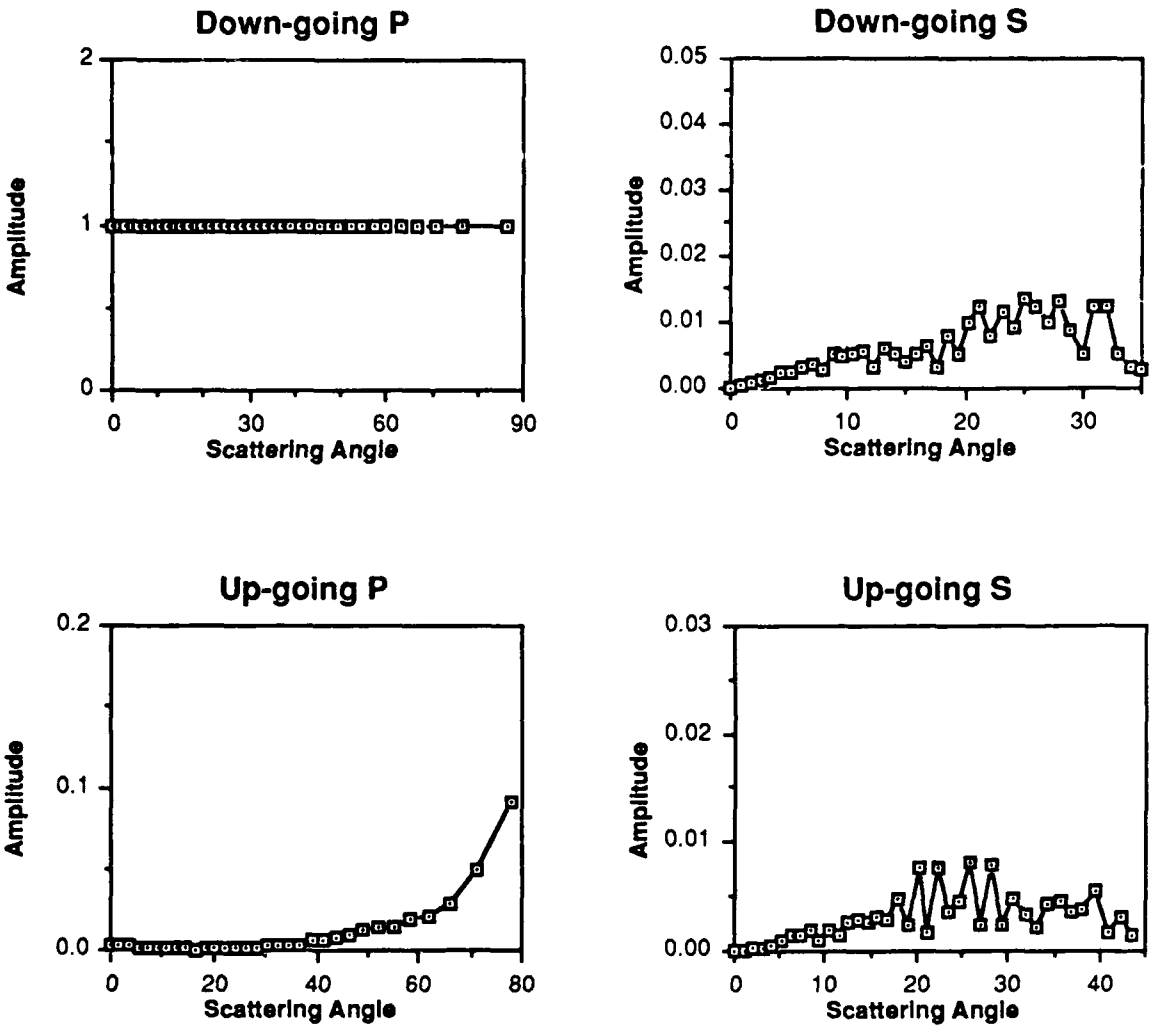

Figure 5: These plots of the wave amplitudes incident on the interface provide a measure of the error versus angle. For each wavenumber, the coefficients are normalized by the amplitude of the down-going P wave source. Hence, the down-going P wave coefficient has unit amplitude for all angles. The remaining three coefficients plotted here are non-physical, and are indicative of error in the conversion of the measured finite difference displacements and stresses into wave coefficients.

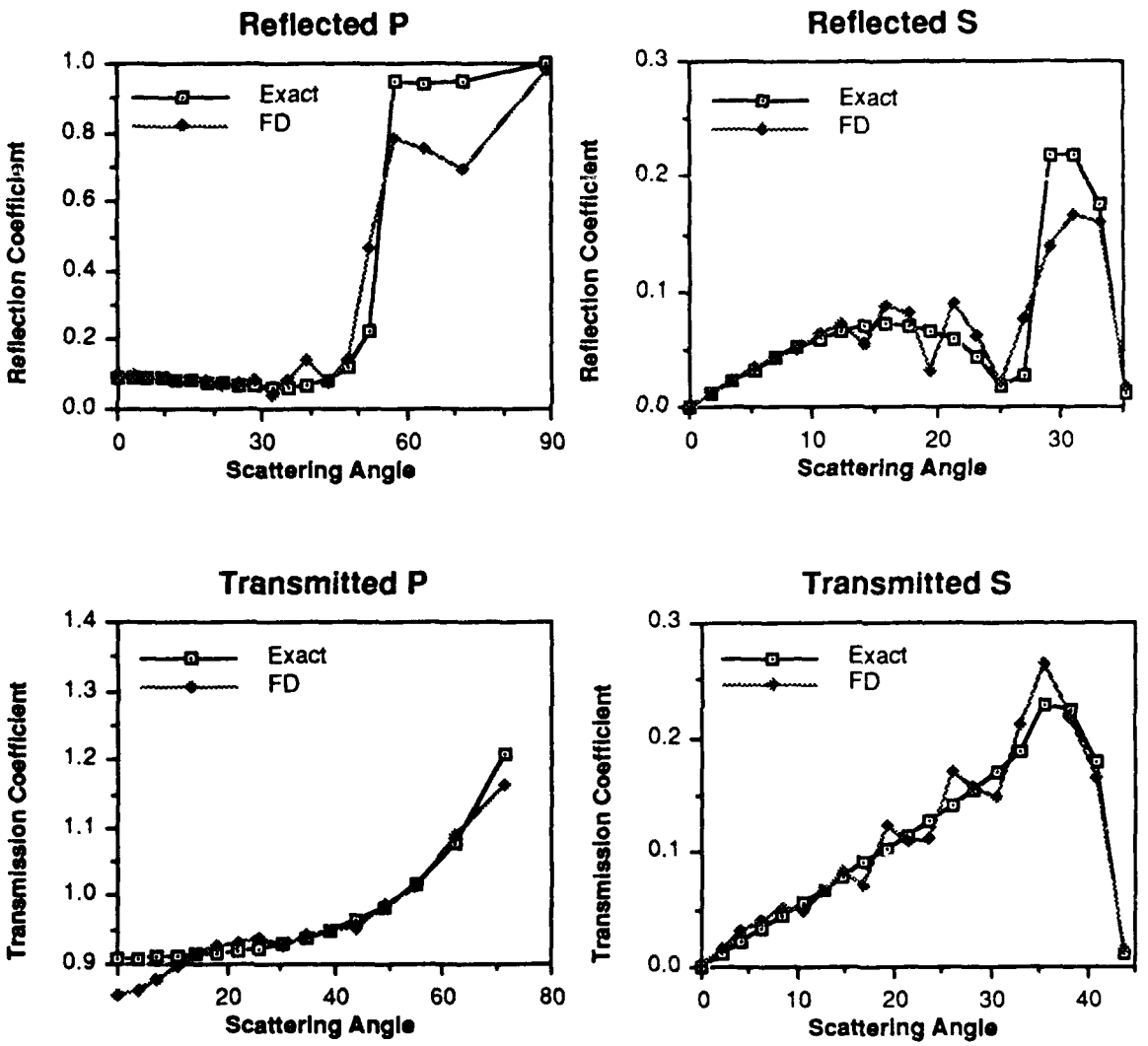

Figure 6: Comparison between P and S wave reflection and transmission coefficients generated by finite difference and analytic methods. The finite difference model is identical to the previous model (*in Figure 3*) except that the grid dimensions and recever array sizes are doubled. The receiver spacing is unchanged. The only effect is to double the aperture of the receiver array. The result is to amplify the "Gibb's ringing" effect of the Figure 4 results.

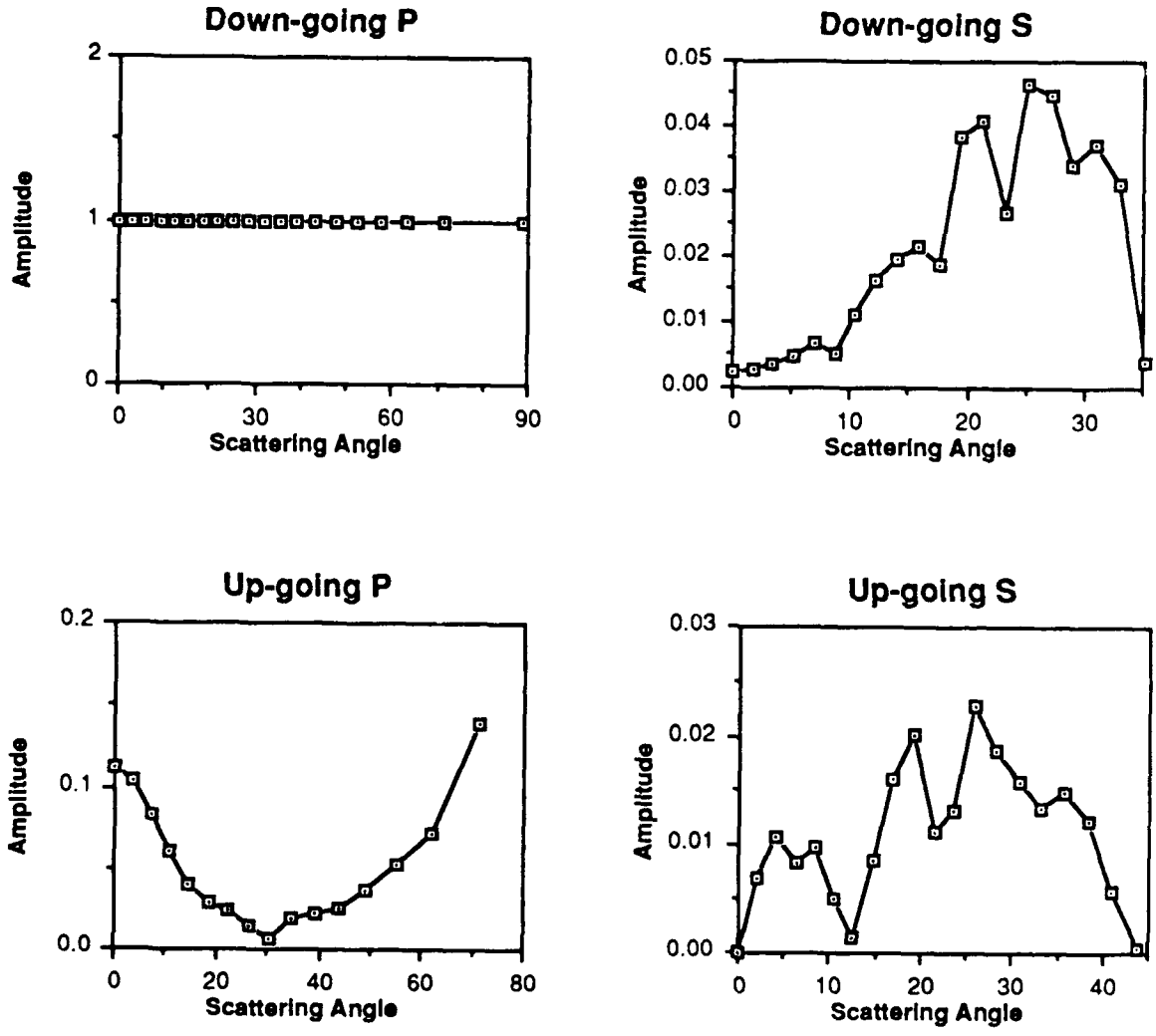

Figure 7: Amplitudes of waves incident on the interface corresponding to the scattered [illegible] amplitudes shown in Figure 6. These are provided as a measure of the error versus [illegible]

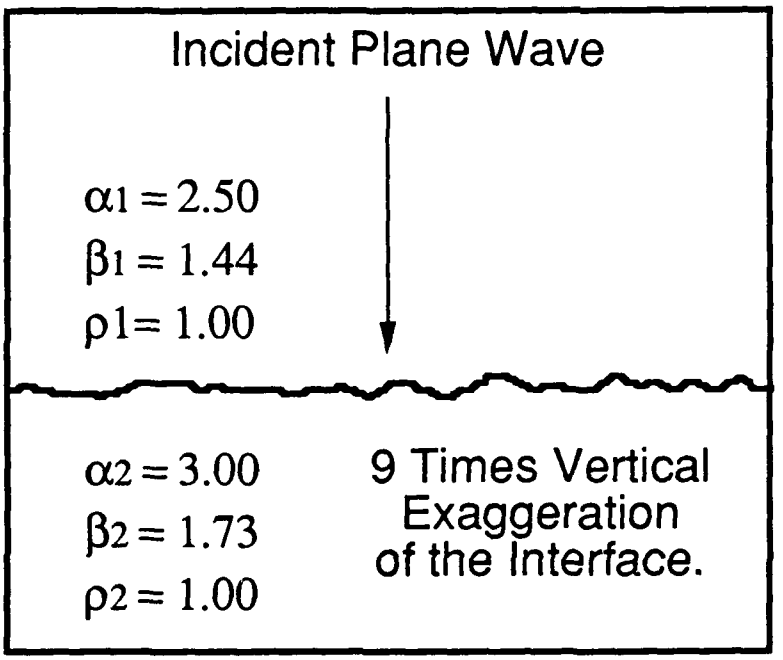

Figure 8: Two-dimensional rough interface model used to compare a perturbation solution with a finite difference solution. The source is a normally incident, 18 Hz, plane wave. The rough interface has a Gaussian autocorrelation function with a correlation length of $L = 100$ m and an rms height deviation of $\sigma = 16.7$ m. The interface is periodic with a period of 2.70 km, the width of the model above. The sampling parameters, $\Delta x = 6.67$ m, $\Delta z = 2.22$ m,and $\Delta t = 0.00156$ s, result in a maximum phase dispersion error of -1.1 percent at 18 Hz. The two receiver arrays are located as close to the interface as is possible without intersection. The horizontal receiver interval equals Δx. All waves within the seismogram time window are contained within the finite difference grid, eliminating the need for absorbing boundaries.

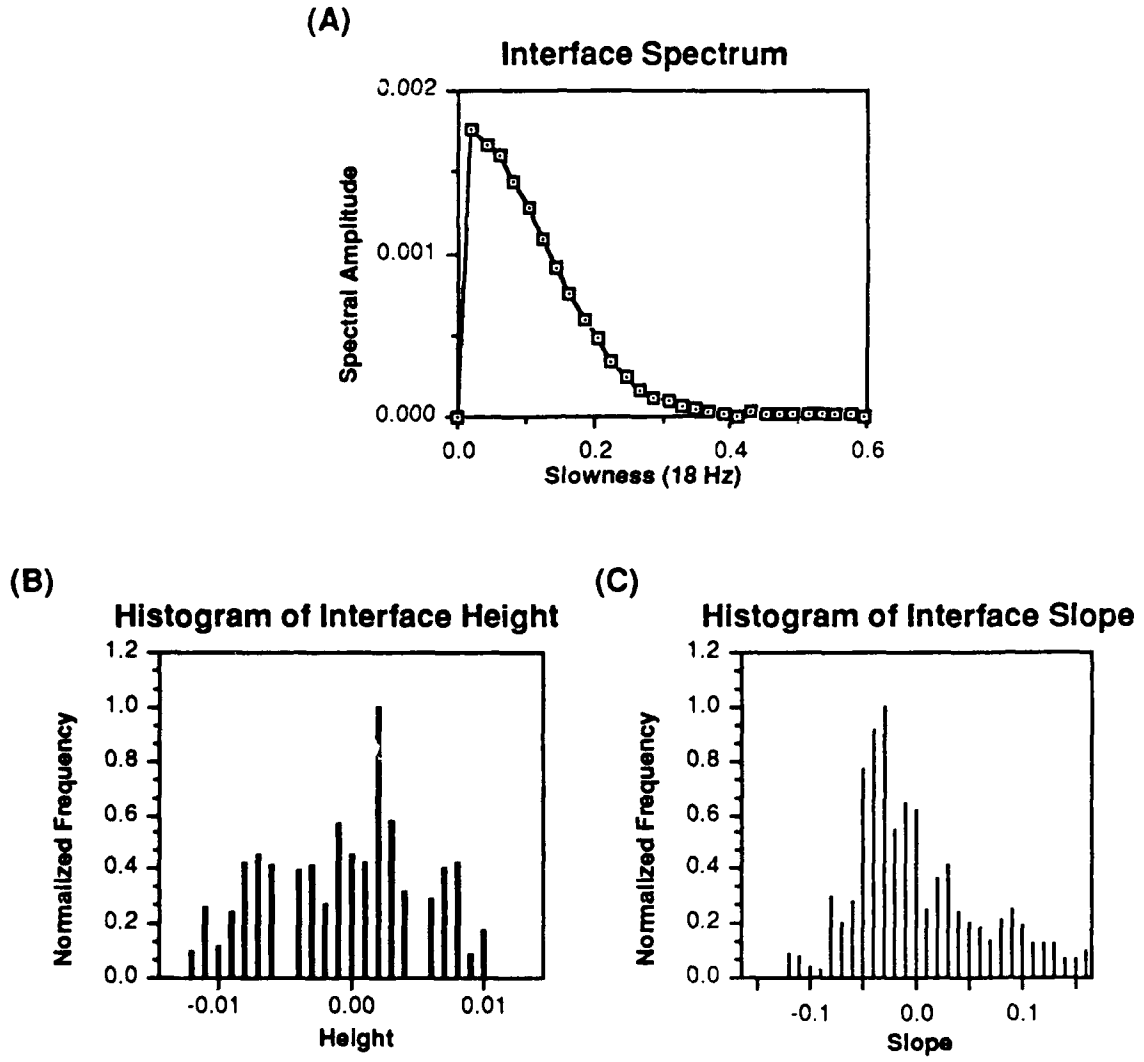

Figure 9: Properties of of the interface shown in Figure 8: (a) Fourier transform, where the horizontal slowness is evaluated for 18 Hz, and histograms of (b) interface height and (c) interface slope.

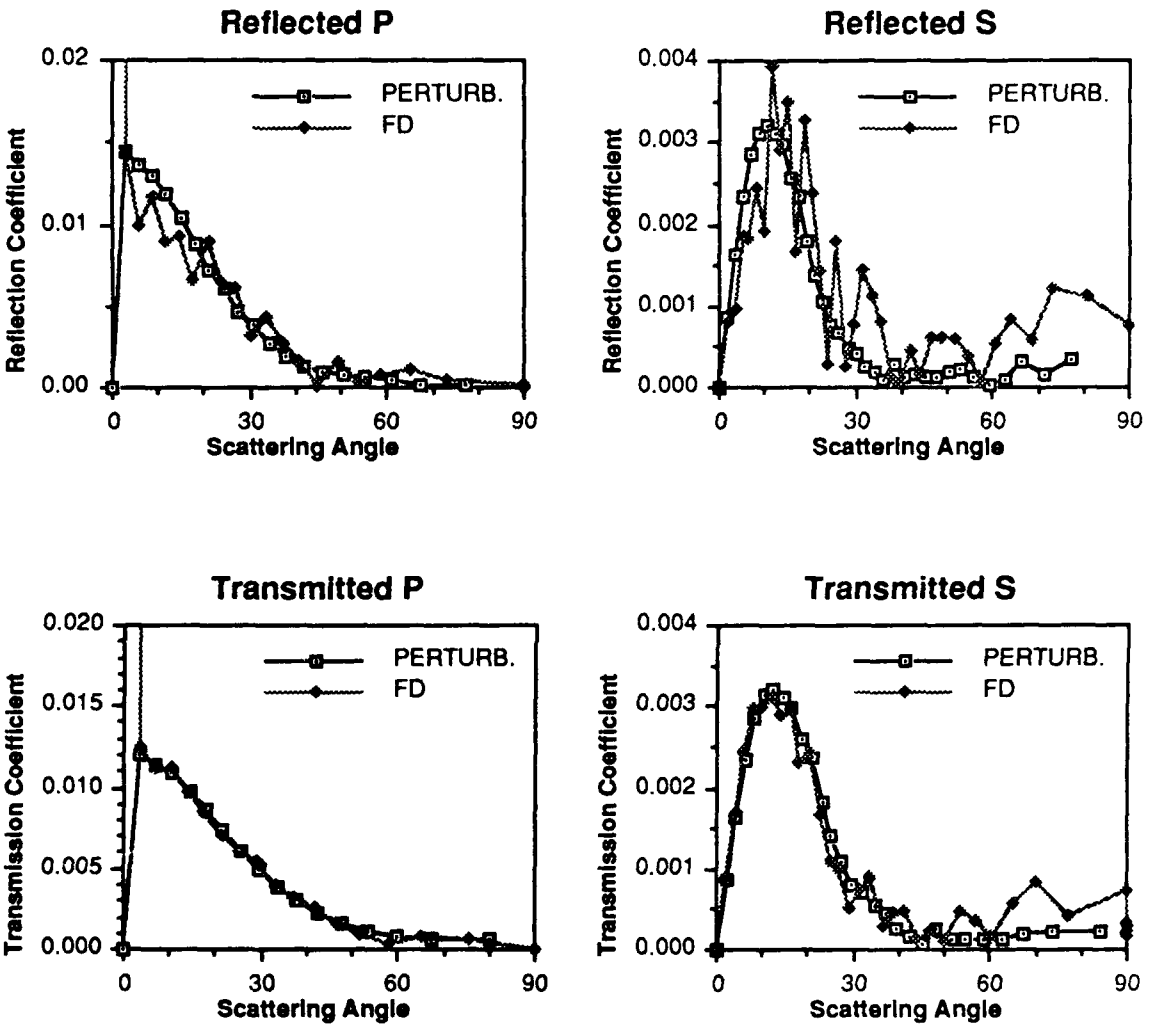

Figure 10: Comparison between P and S wave reflection and transmission coefficients generated from the finite difference and perturbation methods for the model shown in Figure 8.

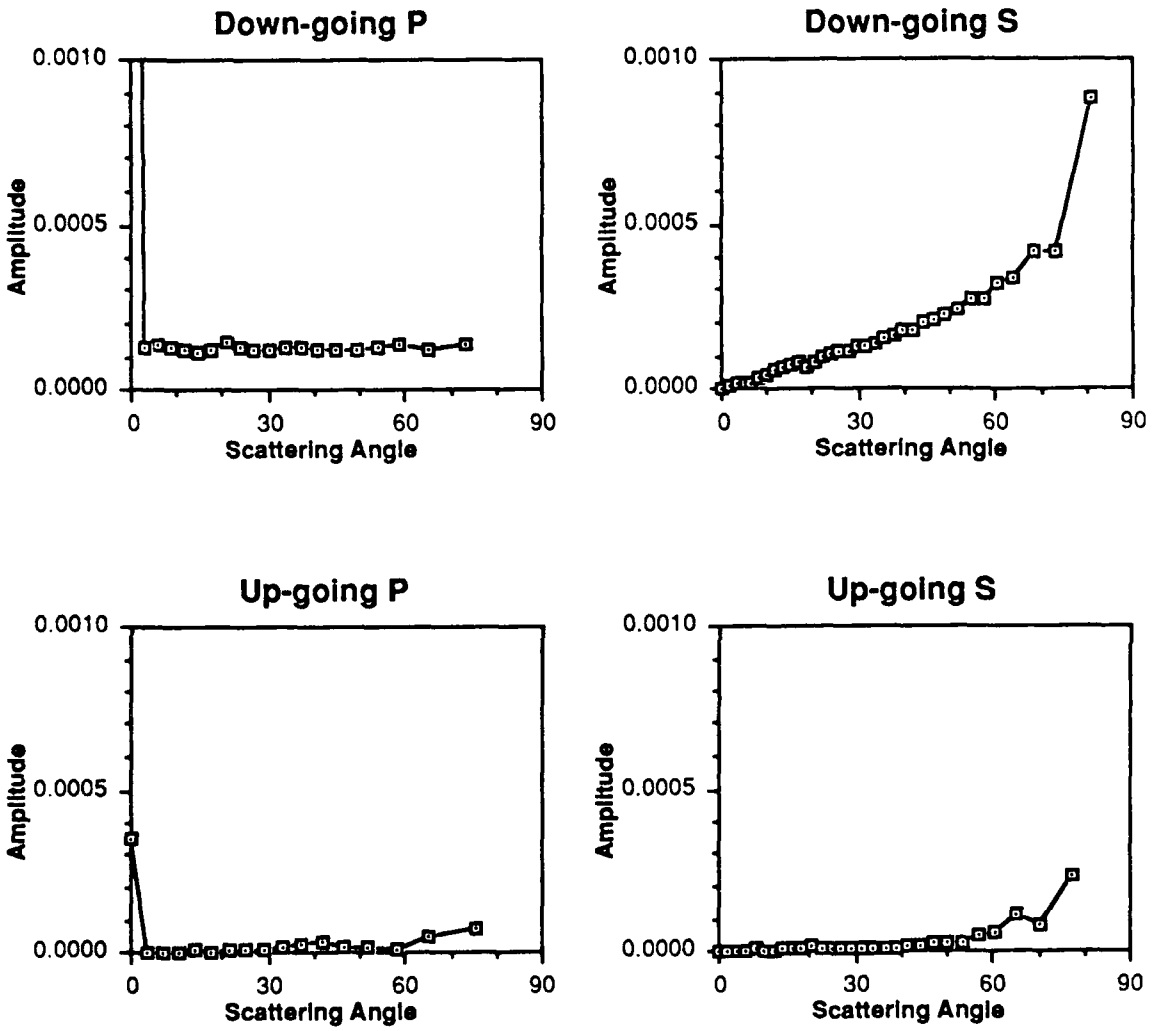

Figure 11: Amplitudes of waves incident on the interface corresponding to the scattered wave amplitudes shown in Figure 10. These are provided as a measure of the error versus angle. The down-going P wave in the upper medium has unit amplitude at zero angle.

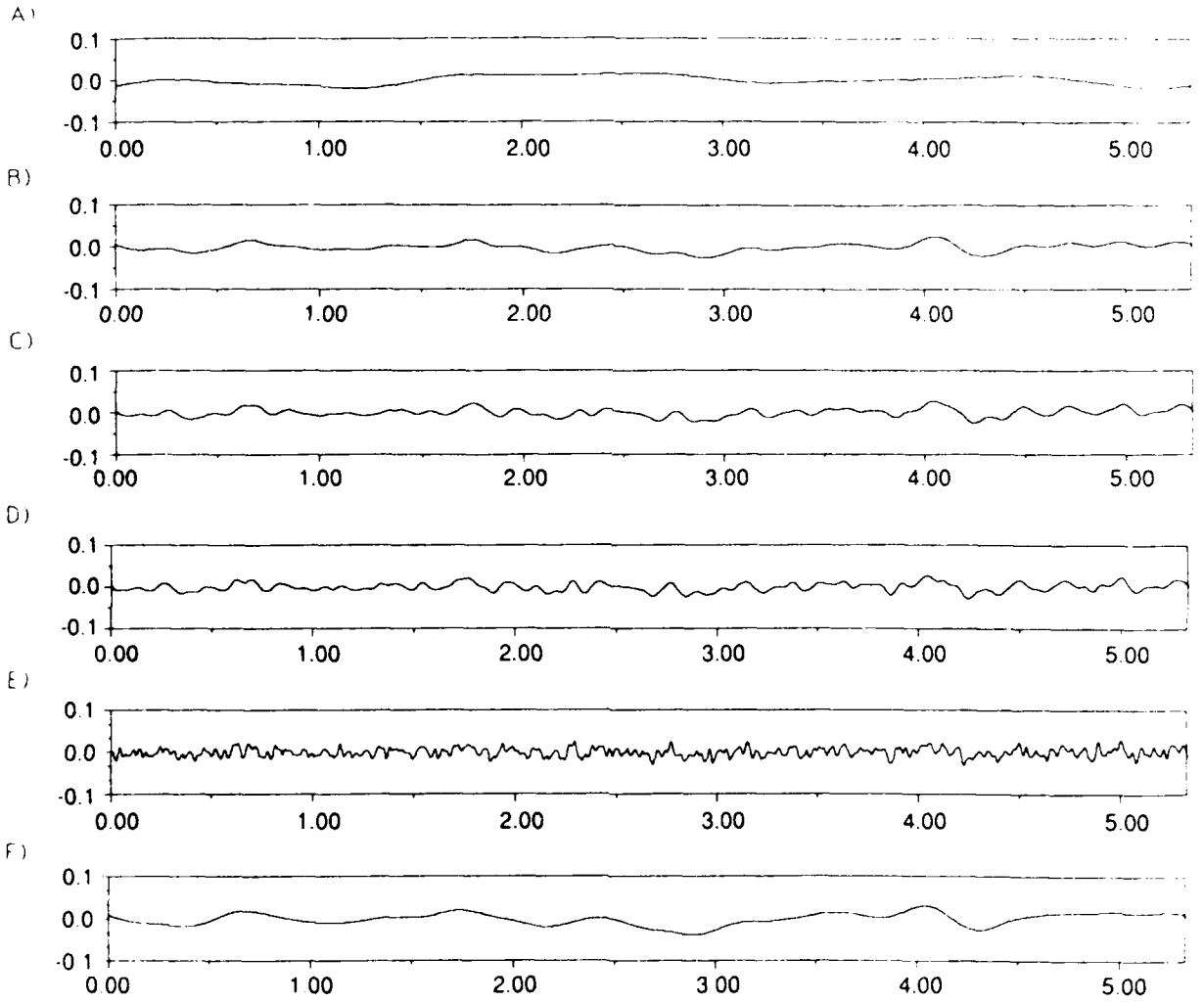

Figure 12: Interface functions used in comparison of reflection and transmission coefficients derived from the perturbation method with those derived from the finite difference method. The interfaces have a Gaussian autocorelation function with RMS height, correlation length, and RMS slope for each interface listed in Table 1.

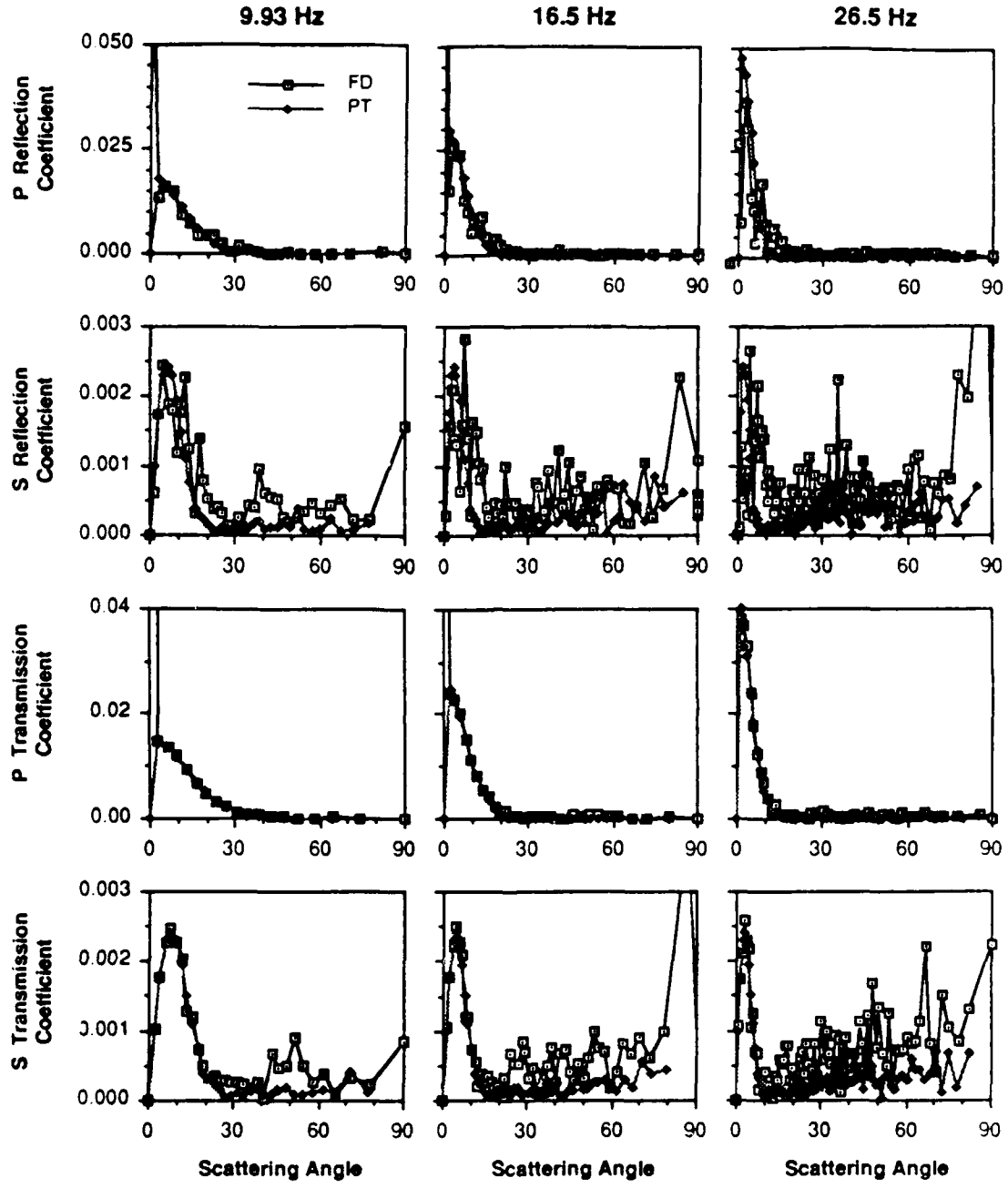

Figure 13a: Comparison of reflection and transmission coefficients derived from the perturbation and finite difference methods for model A. The parameters of the rough interface are given in Table 1 and the interface function is illustrated in Figure 12.

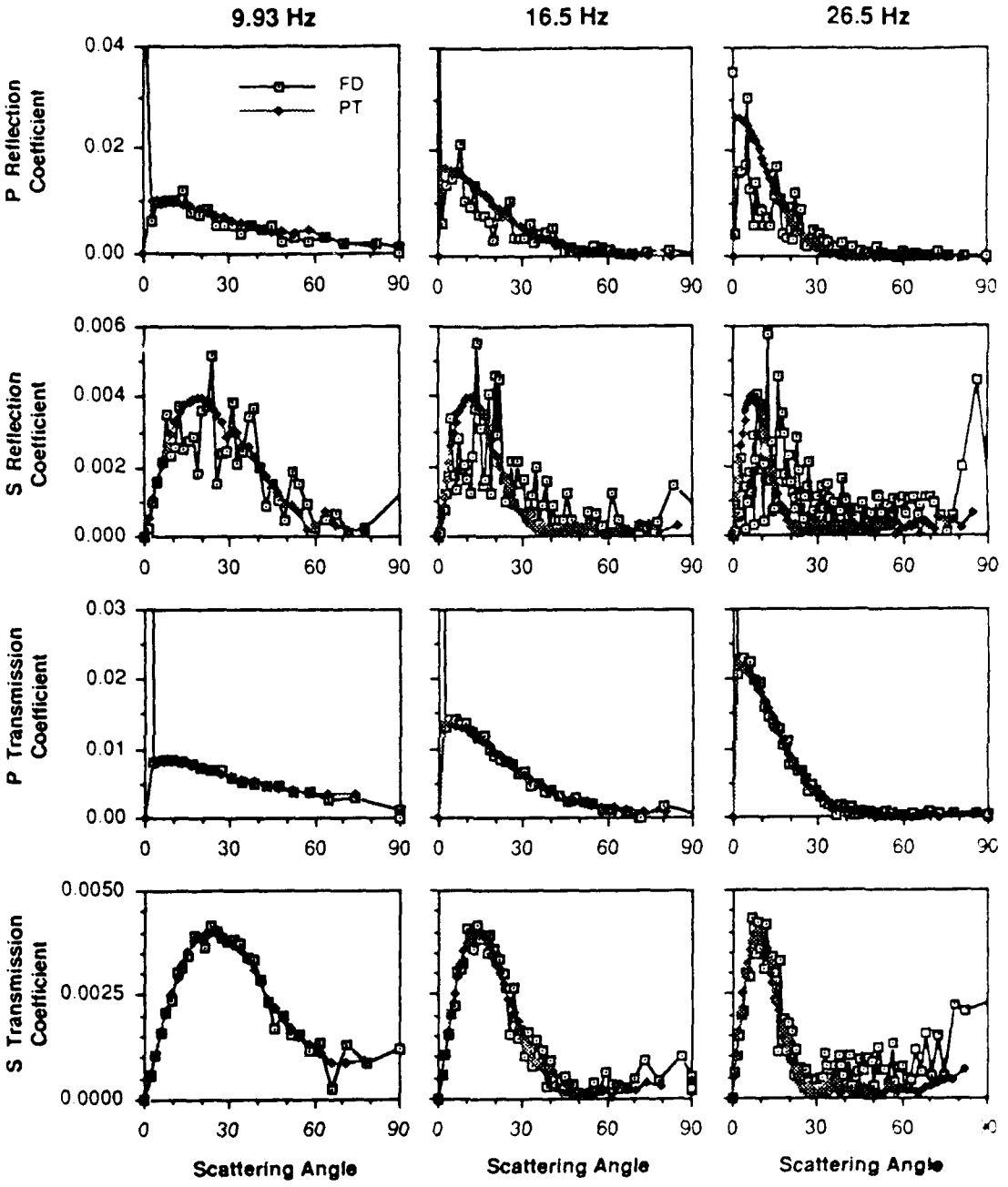

Figure 13b: Comparison of reflection and transmission coefficients derived from the perturbation and finite difference methods for model B. The parameters of the rough interface are given in Table 1 and the interface function is illustrated in Figure 12.

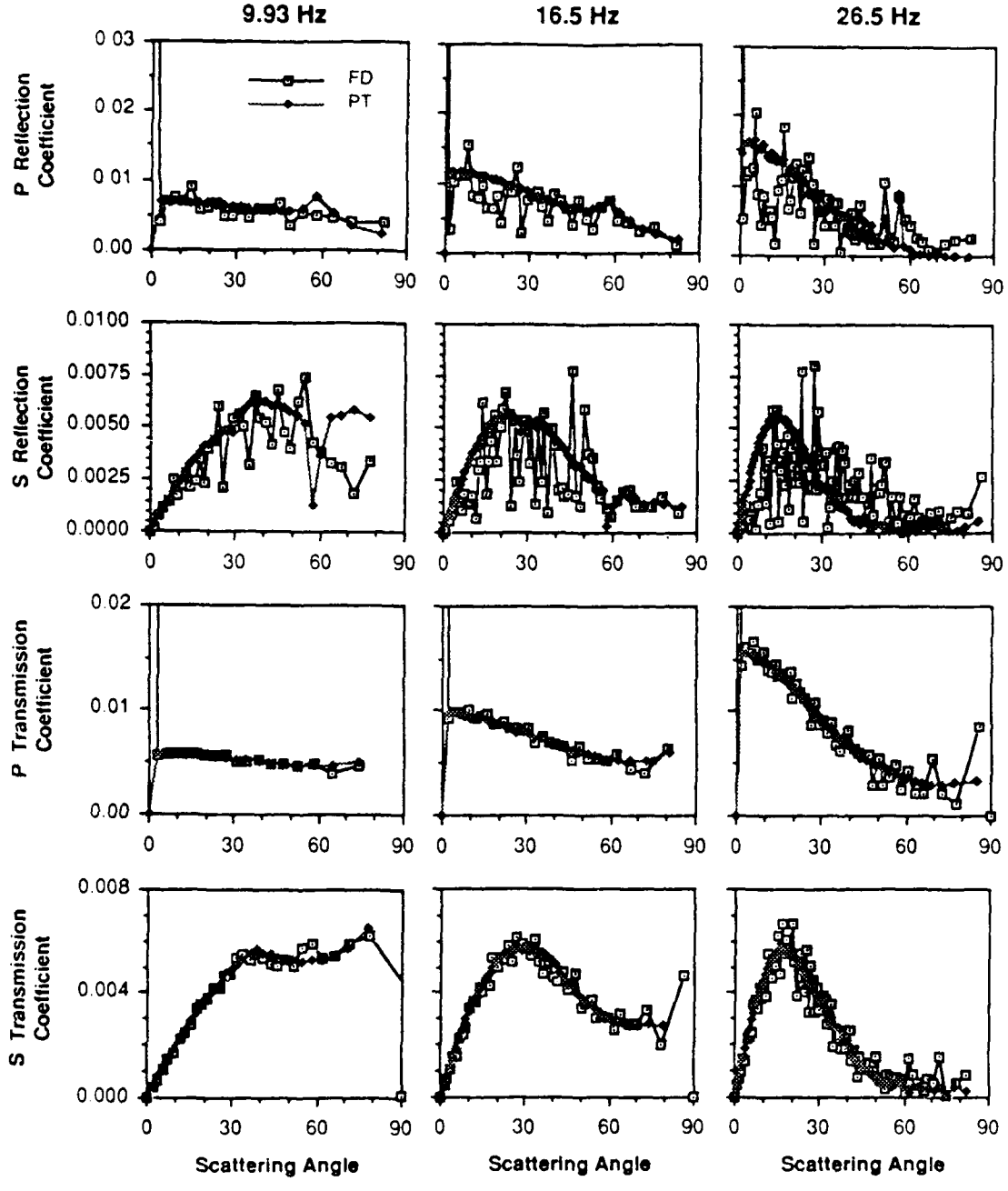

Figure 13c: Comparison of reflection and transmission coefficients derived from the perturbation and finite difference methods for model C. The parameters of the rough interface are given in Table 1 and the interface function is illustrated in Figure 12.

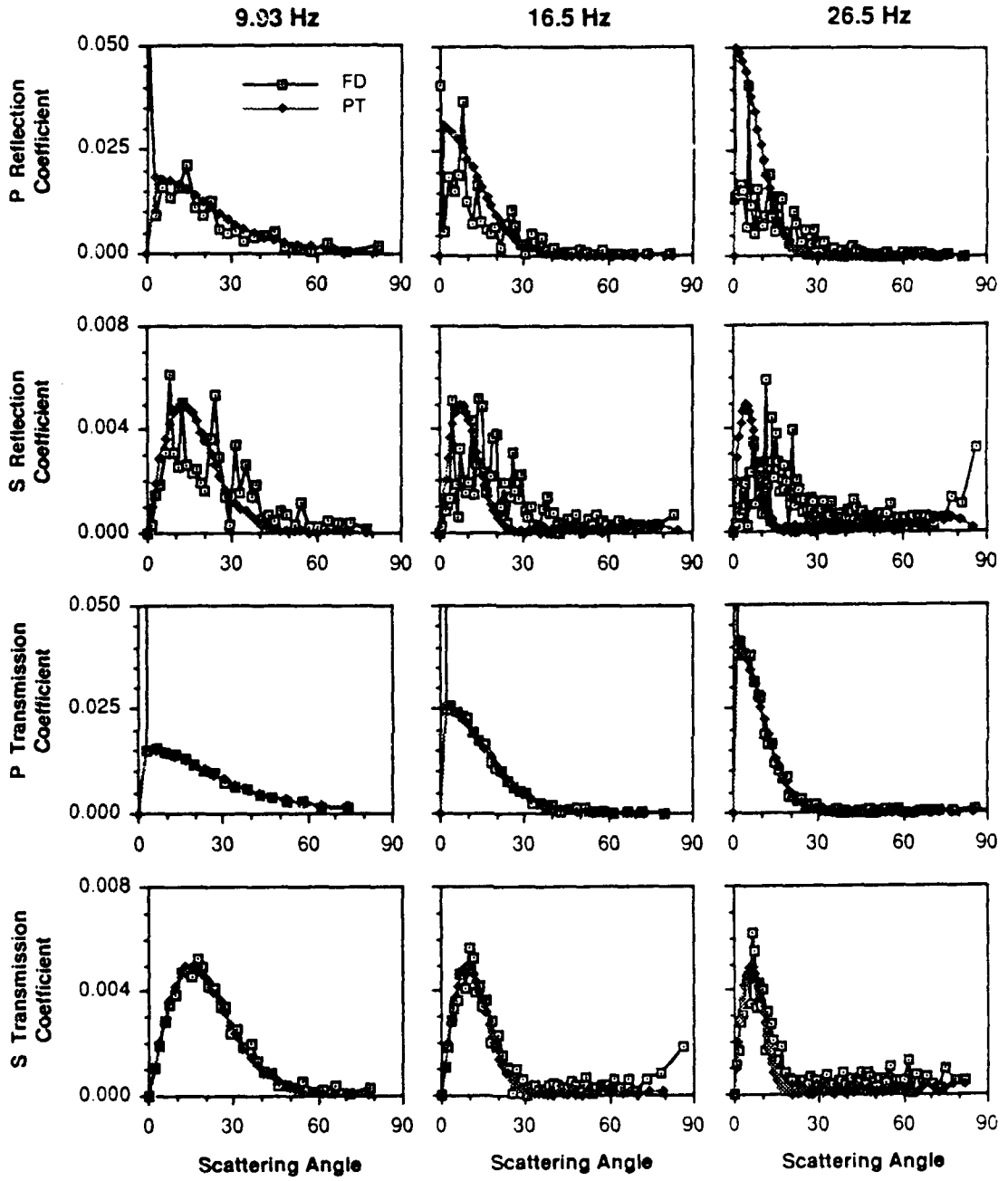

Figure 13d: Comparison of reflection and transmission coefficients derived from the perturbation and finite difference methods for model D. The parameters of the rough interface are given in Table 1 and the interface function is illustrated in Figure 12.

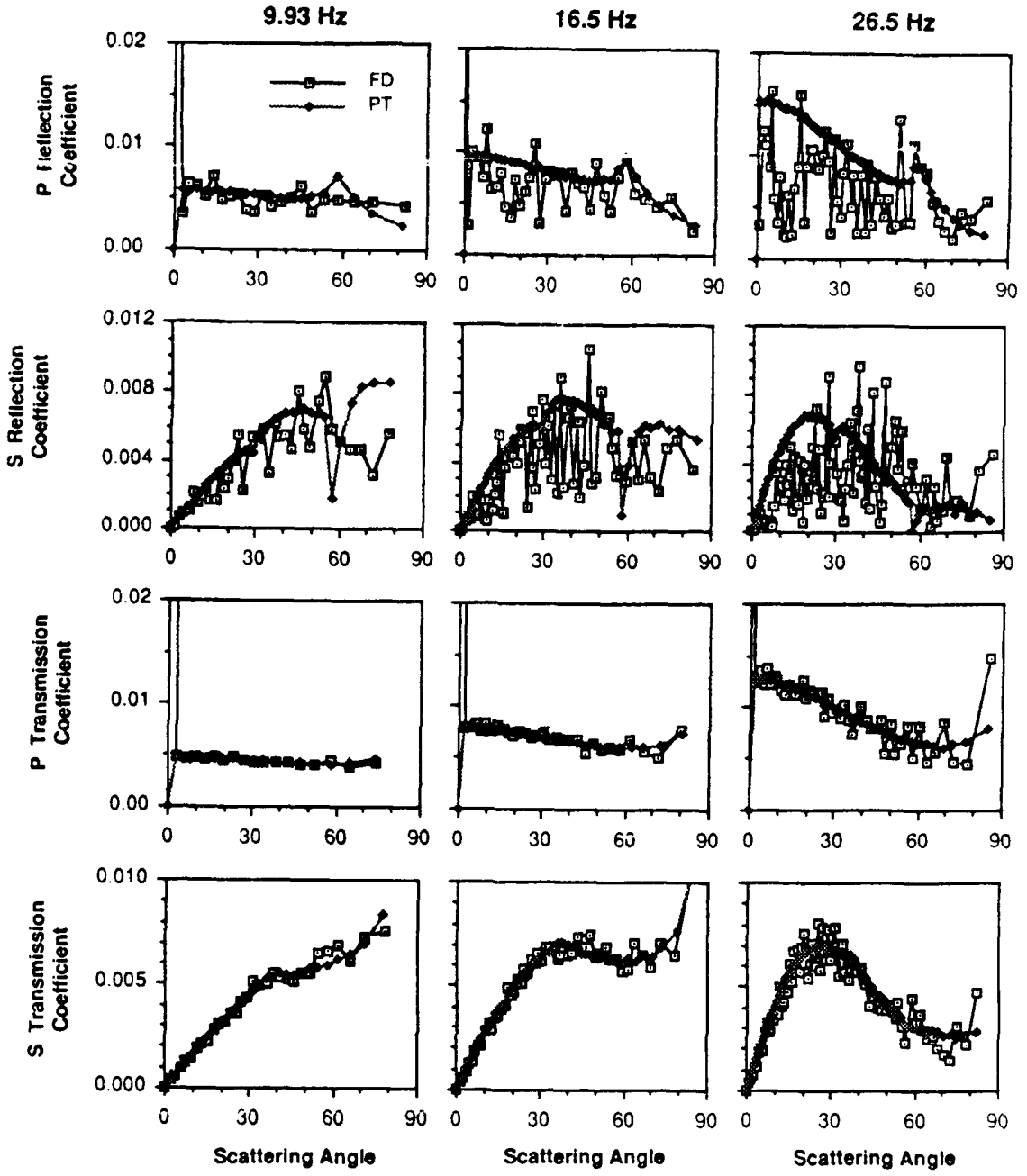

Figure 13c: Comparison of reflection and transmission coefficients derived from the perturbation and finite difference methods for model E. The parameters of the rough interface are given in Table 1 and the interface function is illustrated in Figure 12.

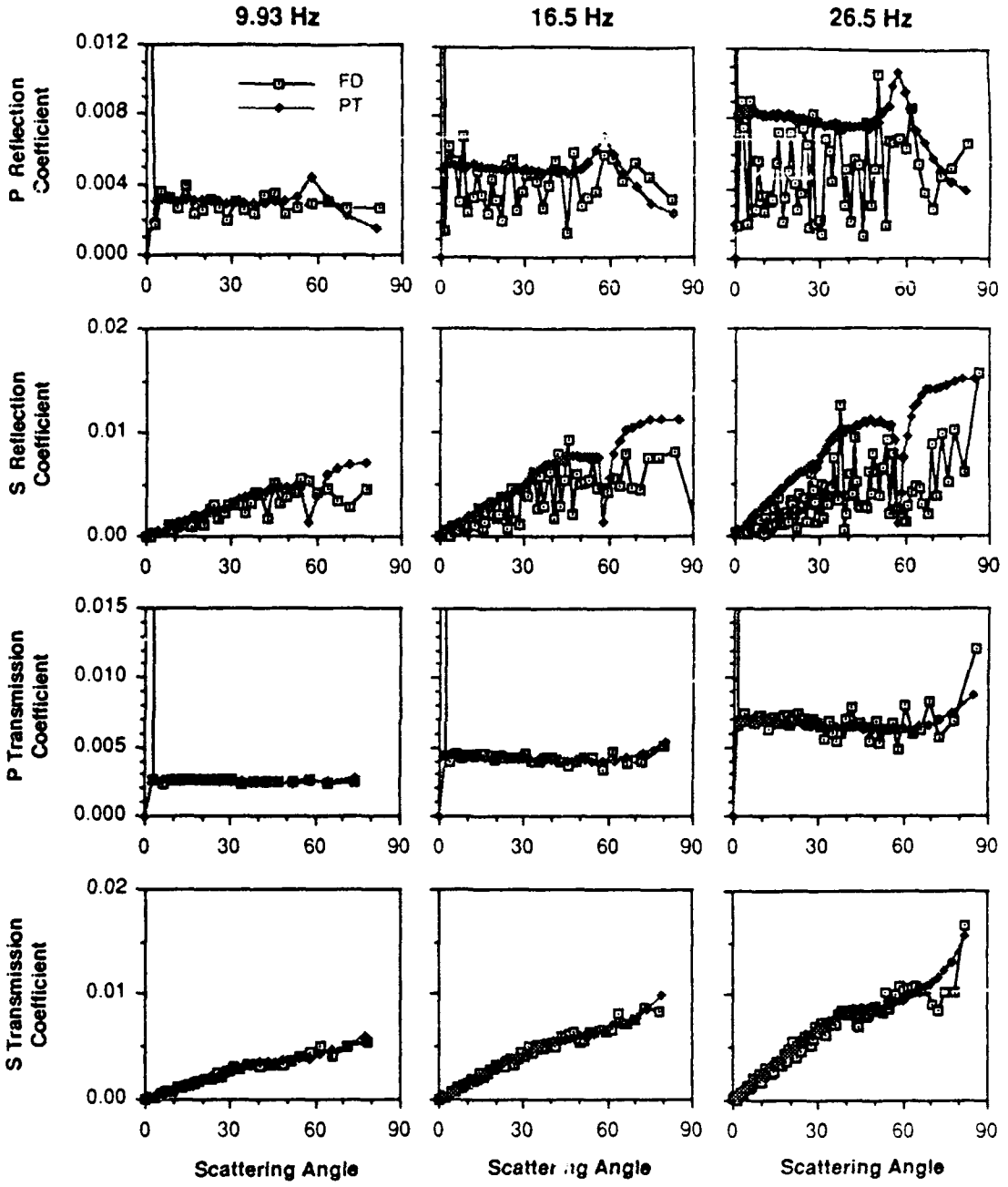

Figure 13f: Comparison of reflection and transmission coefficients derived from the perturbation and finite difference methods for model F. The parameters of the rough interface are given in Table 1 and the interface function is illustrated in Figure 12.

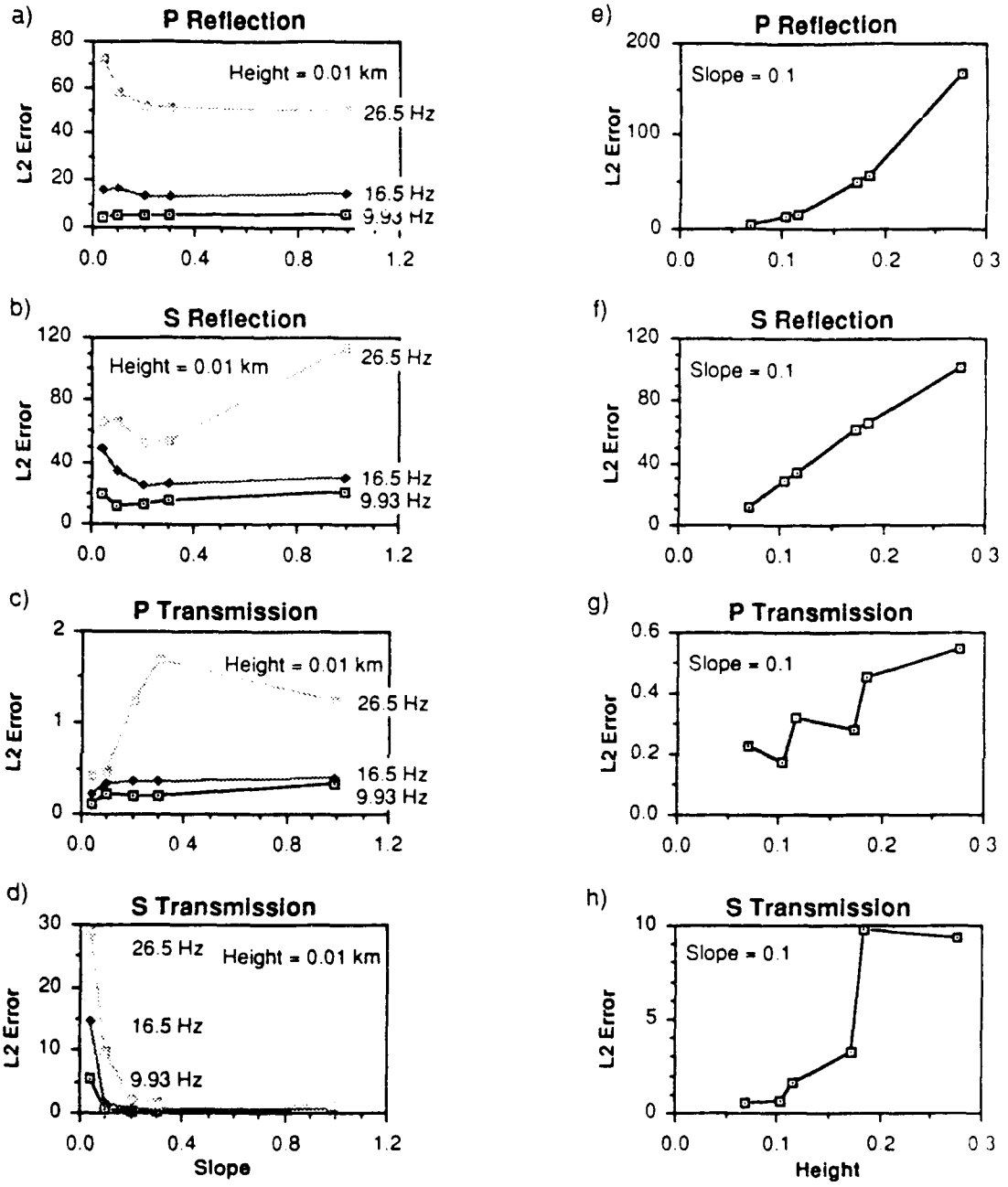

Figure 14: L_2 norm comparison of finite difference and perturbation method derived reflection and transmission coefficients. (a-d) RMS interface height is a constant 0.01 km and RMS slope varies from 0.037 to 0.99. RMS interface height for three frequencies can be expressed as 0.069, 0.11, and 0.18 S_1 wavelengths. (e-h) RMS interface slope is a constant 0.1 and with RMS interface height varies from 0.069 to 0.28 S_1 wavelengths.

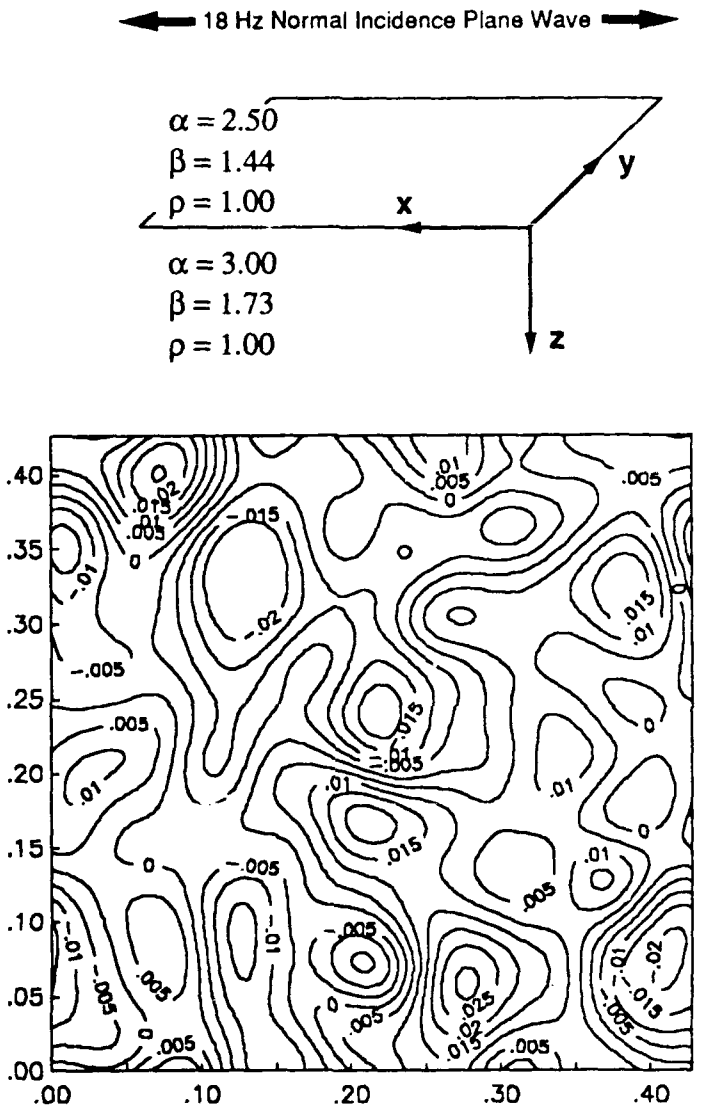

Figure 15: Three-dimensional rough interface scattering model. The auto-correlation function of the interface is a two-dimensional Gaussian with x and y correlation lengths of 2.4 S_1 wavelengths (0.19 km), an RMS height of 0.125 S_1 wavelengths (0.010 km), and an RMS slope of 0.30. Contours and axes are labeled in kilometers.

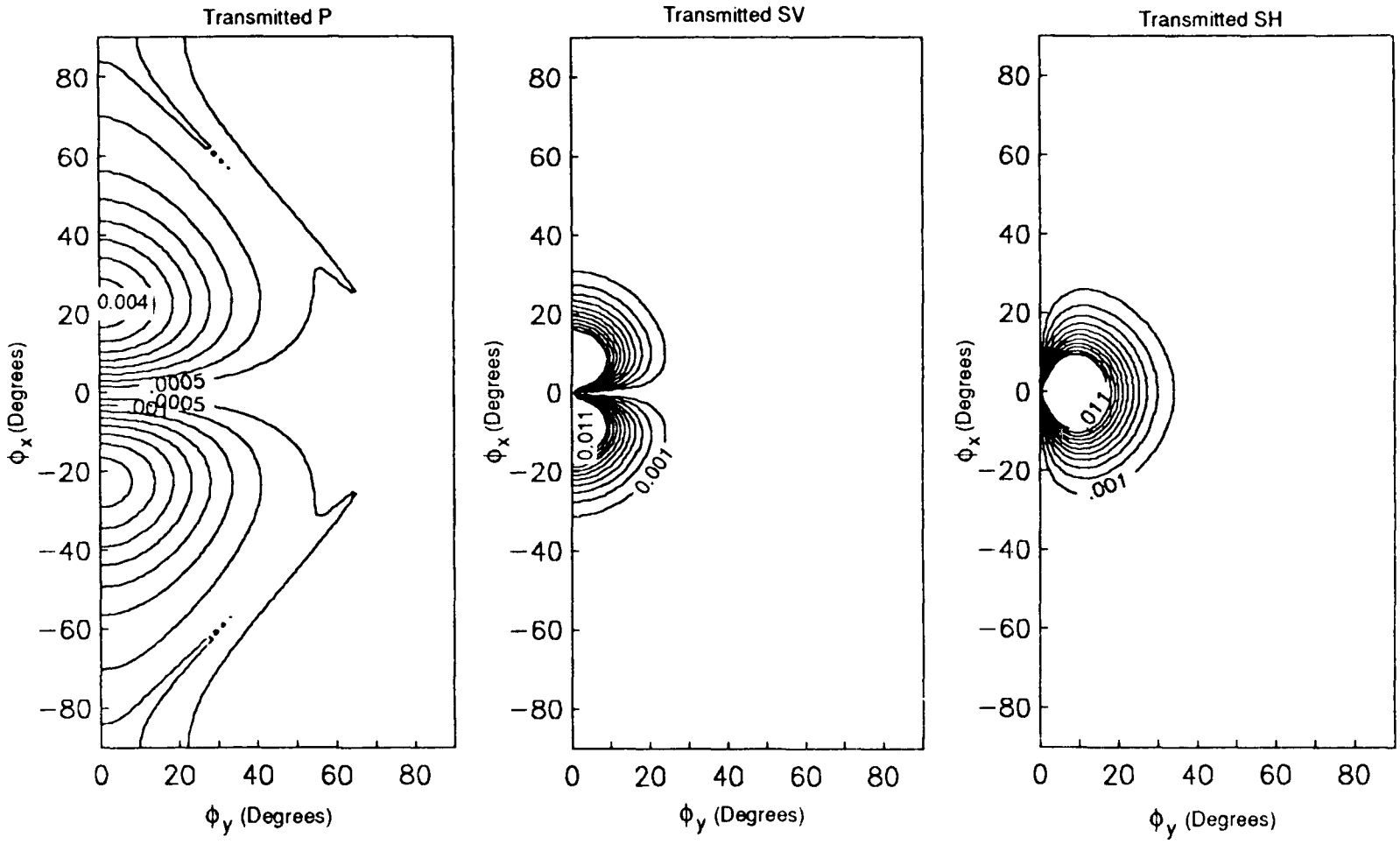

Figure 16: Transmission coefficients for the model in Figure 15. The source is an 18 Hz SV plane wave at normal incidence with particle motion in the x-direction.

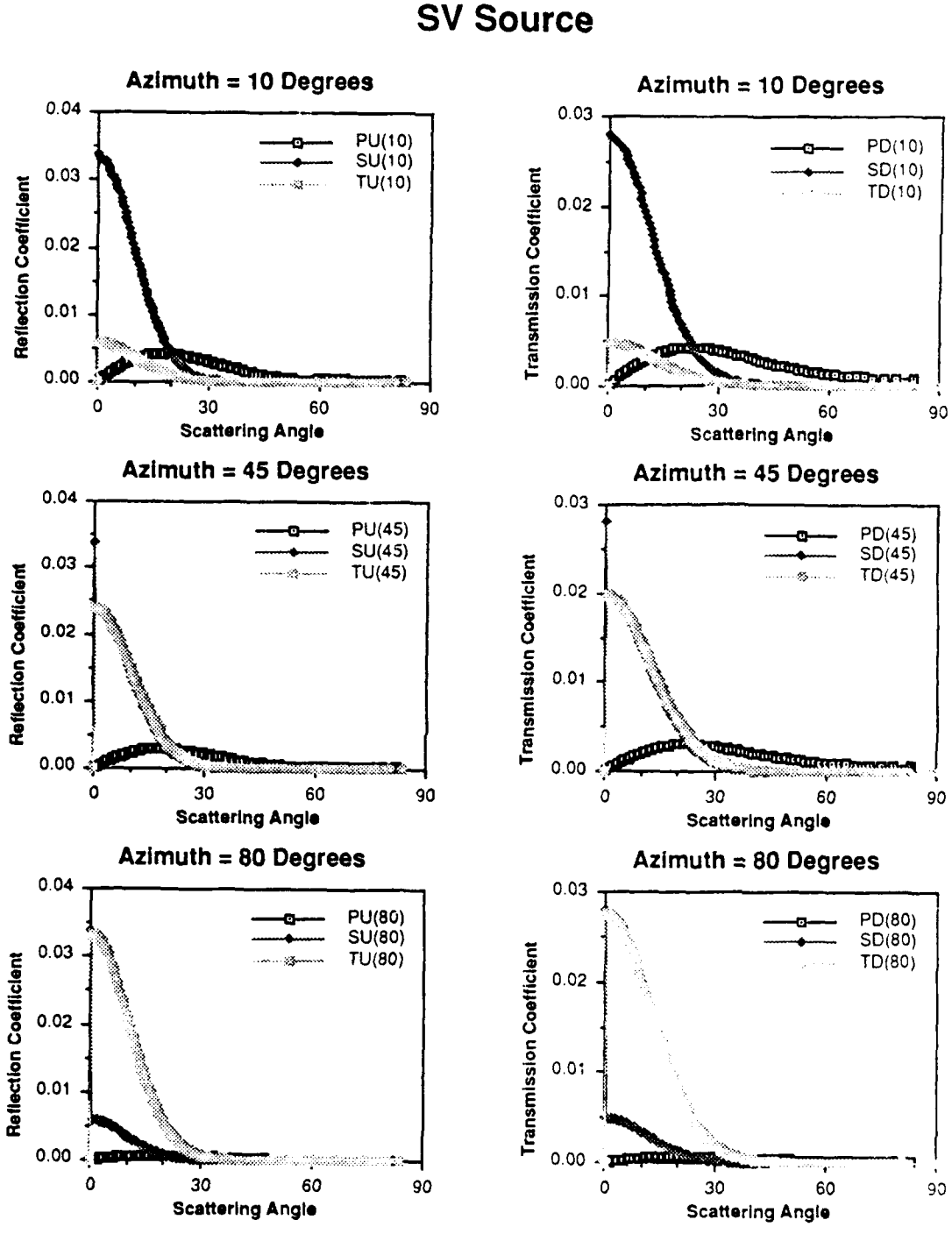

Figure 17: Cross-sections of the transmission coefficients in Figure 16 along 10°, 45°, and 80°azimuths. Reflection coefficients for the same model are also shown.

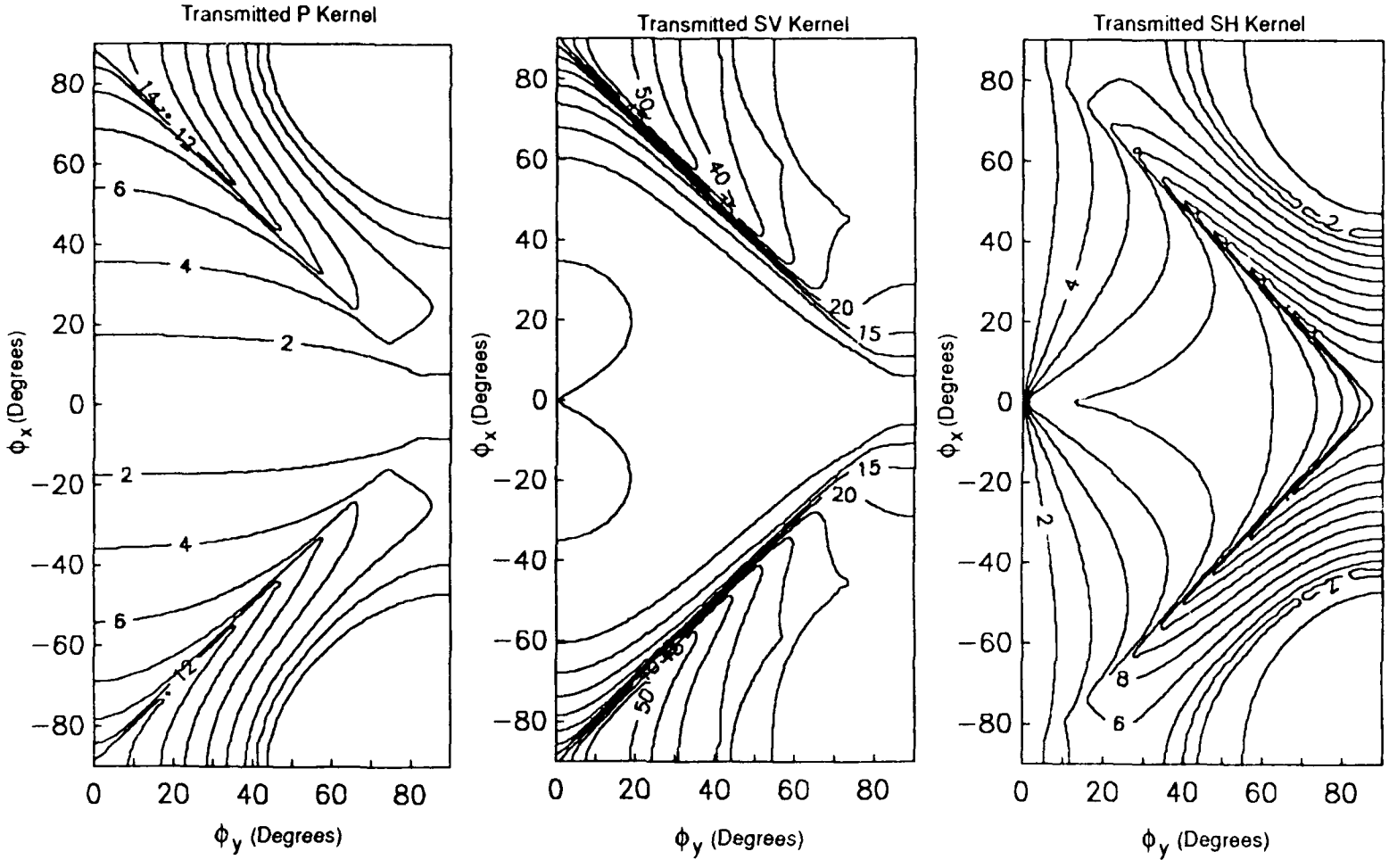

Figure 18: Transmission scattering kernels for the model in Figure 15.

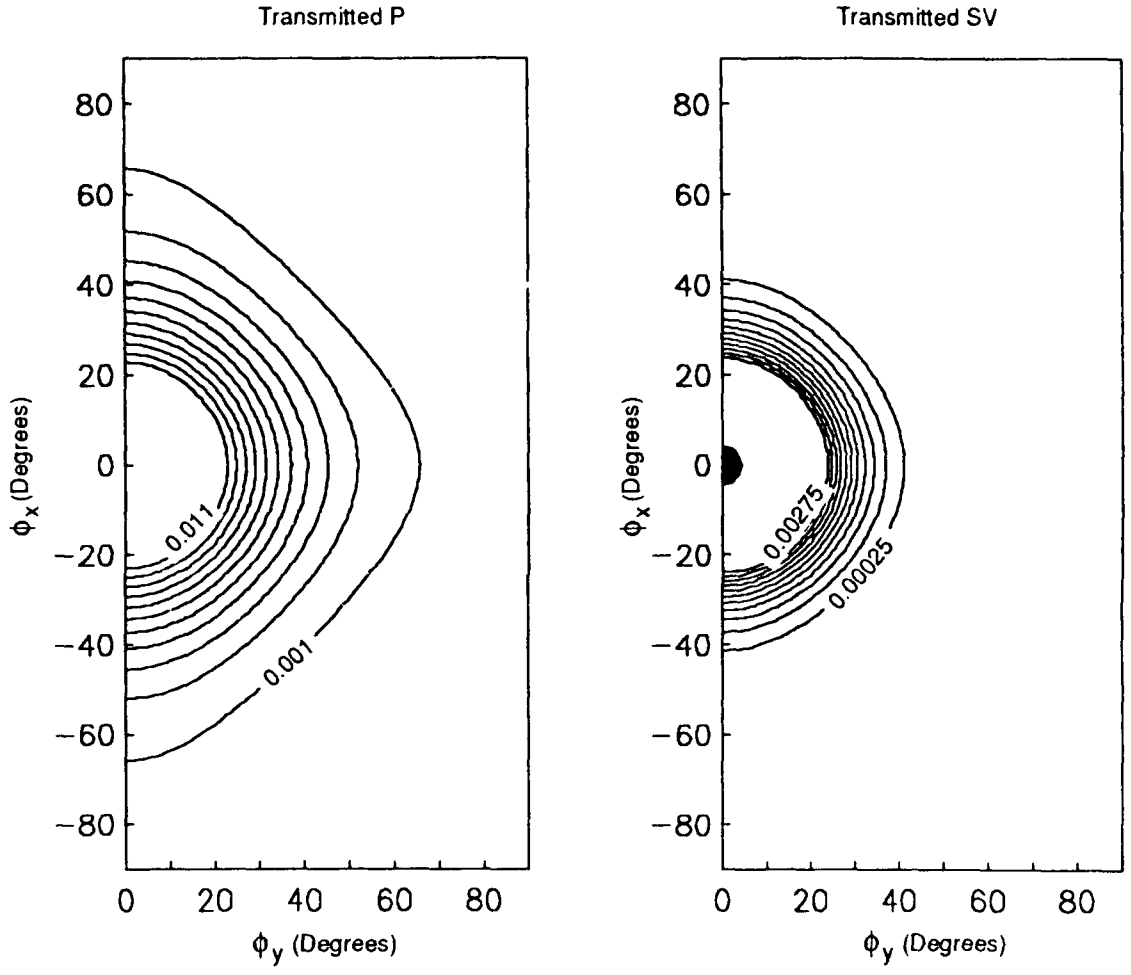

Figure 19: Transmission coefficients for the model in Figure 15. The source is an 18 Hz P plane wave at normal incidence.

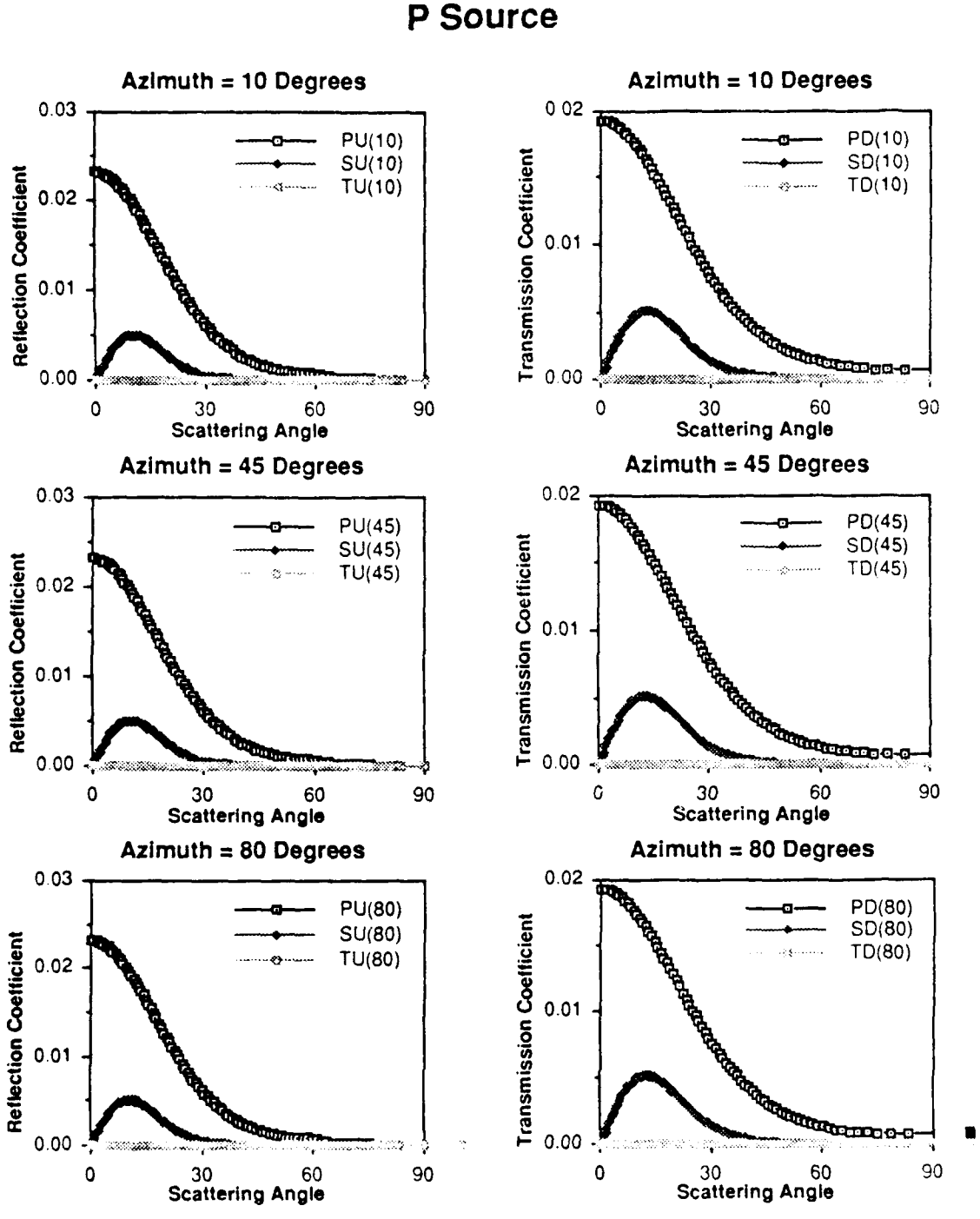

Figure 20: Cross-sections of the transmission coefficients in Figure 19 along 10°, 45°, and 80°azimuths. Reflection coefficients for the same model are also shown.

CONTRACTORS (United States)

Professor Keiiti Aki
Center for Earth Sciences
University of Southern California
University Park
Los Angeles, CA 90089-0741

Professor Charles B. Archambeau
Cooperative Institute for Resch
in Environmental Sciences
University of Colorado
Boulder, CO 80309

Dr. Thomas C. Bache Jr.
Science Applications Int'l Corp.
10210 Campus Point Drive
San Diego, CA 92121 (2 copies)

Dr. Douglas R. Baumgardt
Signal Analysis & Systems Div.
ENSCO, Inc.
5400 Port Royal Road
Springfield, VA 22151-2388

Dr. Jonathan Berger
Institute of Geophysics and
Planetary Physics
Scripps Institution of Oceanography
A-025
University of California, San Diego
La Jolla, CA 92093

Dr. S. Bratt
Science Applications Int'l Corp.
10210 Campus Point Drive
San Diego, CA 92121

Dr. Lawrence J. Burdick
Woodward-Clyde Consultants
P.O. Box 93245
Pasadena, CA 91109-3245 (2 copies)

Professor Robert W. Clayton
Seismological Laboratory/Div. of
Geological & Planetary Sciences
California Institute of Technology
Pasadena, CA 91125

Dr Karl Coyner
N. E. Research
P.O. Box 857
Norwich, VT 05055

Dr. Vernon F. Cormier
Department of Geology & Geophysics
U-45, Roon 207
The University of Conneticut
Storrs, Connecticut 06268

Dr. Steven Day
Dept. of Geological Sciences
San Diego State U.
San Diego, CA 92182

Dr. Zoltan A. Der
ENSCO, Inc.
5400 Port Royal Road
Springfield, VA 22151-2388

Professor John Ferguson
Center for Lithospheric Studies
The University of Texas at Dallas
P.O. Box 830688
Richardson, TX 75083-0688

Professor Stanley Flatte'
Applied Sciences Building
University of California,
Santa Cruz, CA 95064

Dr. Alexander Florence
SRI International
333 Ravenswood Avenue
Menlo Park, CA 94025-3493

Professor Steven Grand
Department of Geology
245 Natural History Building
1301 West Green Street
Urbana, IL 61801

Dr. Henry L. Gray
Associate Dean of Dedman College
Department of Statistical Sciences
Southern Methodist University
Dallas, TX 75275

Professor Roy Greenfield
Geosciences Department
403 Deike Building
The Pennsylvania State University
University Park, PA 16802

Professor David G. Harkrider
Seismological Laboratory
Div of Geological & Planetary Sciences
California Institute of Technology
Pasadena, CA 91125

Professor Donald V. Helmberger
Seismological Laboratory
Div of Geological & Planetary Sciences
California Institute of Technology
Pasadena, CA 91125

Professor Eugene Herrin
Institute for the Study of Earth
& Man/Geophysical Laboratory
Southern Methodist University
Dallas, TX 75275

Professor Robert B. Herrmann
Department of Earth & Atmospheric
Sciences
Saint Louis University
Saint Louis, MO 63156

Professor Bryan Isacks
Cornell University
Dept of Geological Sciences
SNEE Hall
Ithaca, NY 14850

Professor Lane R. Johnson
Seismographic Station
University of California
Berkeley, CA 94720

Professor Thomas H. Jordan
Department of Earth, Atmospheric
and Planetary Sciences
Mass Institute of Technology
Cambridge, MA 02139

Dr. Alan Kafka
Department of Geology &
Geophysics
Boston College
Chestnut Hill, MA 02167

Professor Leon Knopoff
University of California
Institute of Geophysics
& Planetary Physics
Los Angeles, CA 90024

Professor Charles A. Langston
Geosciences Department
403 Deike Building
The Pennsylvania State University
University Park, PA 16802

Professor Thorne Lay
Department of Geological Sciences
1006 C.C. Little Building
University of Michigan
Ann Harbor, MI 48109-1063

Dr. Randolph Martin III
New England Research, Inc.
P.O. Box 857
Norwich, VT 05055

Dr. Gary McCartor
Mission Research Corp.
735 State Street
P.O. Drawer 719
Santa Barbara, CA 93102 (2 copies)

Professor Thomas V. McEvilly
Seismographic Station
University of California
Berkeley, CA 94720

Dr. Keith L. McLaughlin
S-CUBED,
A Division of Maxwell Laboratory
P.O. Box 1620
La Jolla, CA 92038-1620

Professor William Menke
Lamont-Doherty Geological Observatory
of Columbia University
Palisades, NY 10964

Professor Brian J. Mitchell
Department of Earth & Atmospheric
Sciences
Saint Louis University
Saint Louis, MO 63156

Mr. Jack Murphy
S-CUBED
A Division of Maxwell Laboratory
11800 Sunrise Valley Drive
Suite 1212
Reston, VA 22091 (2 copies)

Professor J. A. Orcutt
Institute of Geophysics and Planetary
Physics, A-205
Scripps Institute of Oceanography
Univ. of California, San Diego
La Jolla, CA 92093

Professor Keith Priestley
University of Nevada
Mackay School of Mines
Reno, NV 89557

Professor Paul G. Richards
Lamont-Doherty Geological
Observatory of Columbia Univ.
Palisades, NY 10964

Wilmer Rivers
Teledyne Geotech
314 Montgomery Street
Alexandria, VA 22314

Dr. Alan S. Ryall, Jr.
Center of Seismic Studies
1300 North 17th Street
Suite 1450
Arlington, VA 22209-2308 (4 copies)

Professor Charles G. Sammis
Center for Earth Sciences
University of Southern California
University Park
Los Angeles, CA 90089-0741

Professor Christopher H. Scholz
Geological Sciences
Lamont-Doherty Geological Observatory
Palisades, NY 10964

Dr. Jeffrey L. Stevens
S-CUBED,
A Division of Maxwell Laboratory
P.O. Box 1620
La Jolla, CA 92038-1620

Professor Brian Stump
Institute for the Study of Earth & Man
Geophysical Laboratory
Southern Methodist University
Dallas, TX 75275

Professor Ta-liang Teng
Center for Earth Sciences
University of Southern California
University Park
Los Angeles, CA 90089-0741

Dr. Clifford Thurber
State University of New York at
Stony Brooks
Dept of Earth and Space Sciences
Stony Brook, NY 11794-2100

Professor M. Nafi Toksoz
Earth Resources Lab
Dept of Earth, Atmospheric and
Planetary Sciences
Massachusetts Institute of Technology
42 Carleton Street
Cambridge, MA 02142

Professor Terry C. Wallace
Department of Geosciences
Building #11
University of Arizona
Tucson, AZ 85721

Weidlinger Associates
ATTN: Dr. Gregory Wojcik
4410 El Camino Real, Suite 110
Los Altos, CA 94022

Professor Francis T. Wu
Department of Geological Sciences
State University of New York
at Binghamton
Vestal, NY 13901

OTHERS (United States)

Dr. Monem Abdel-Gawad
Rockwell Internat'l Science Center
1049 Camino Dos Rios
Thousand Oaks, CA 91360

Professor Shelton S. Alexander
Geosciences Department
403 Deike Building
The Pennsylvania State University
University Park, PA 16802

Dr. Ralph Archuleta
Department of Geological
Sciences
Univ. of California at
Santa Barbara
Santa Barbara, CA

Dr. Muawia Barazangi
Geological Sciences
Cornell University
Ithaca, NY 14853

J. Barker
Department of Geological Sciences
State University of New York
at Binghamton
Vestal, NY 13901

Mr. William J. Best
907 Westwood Drive
Vienna, VA 22180

Dr. N. Biswas
Geophysical Institute
University of Alaska
Fairbanks, AK 99701

Dr. G. A. Bollinger
Department of Geological Sciences
Virginia Polytechnical Institute
21044 Derring Hall
Blacksburg, VA 24061

Dr. James Bulau
Rockwell Int'l Science Center
1049 Camino Dos Rios
P.O. Box 1085
Thousand Oaks, CA 91360

Mr. Roy Burger
1221 Serry Rd.
Schenectady, NY 12309

Dr. Robert Burridge
Schlumberger-Doll Resch Ctr.
Old Quarry Road
Ridgefield, CT 06877

Science Horizons, Inc.
ATTN: Dr. Theodore Cherry
710 Encinitas Blvd., Suite 101
Encinitas, CA 92024 (2 copies)

Professor Jon F. Claerbout
Professor Amos Nur
Dept. of Geophysics
Stanford University
Stanford, CA 94305 (2 copies)

Dr. Anton W. Dainty
AFGL/LWH
Hanscom AFB, MA 01731

Professor Adam Dziewonski
Hoffman Laboratory
Harvard University
20 Oxford St.
Cambridge, MA 02138

Professor John Ebel
Dept of Geology & Geophysics
Boston College
Chestnut Hill, MA 02167

Dr. Donald Forsyth
Dept. of Geological Sciences
Brown University
Providence, RI 02912

Dr. Anthony Gangi
Texas A&M University
Department of Geophysics
College Station, TX 77843

Dr. Freeman Gilbert
Institute of Geophysics &
Planetary Physics
Univ. of California, San Diego
P.O. Box 109
La Jolla, CA 92037

Mr. Edward Giller
Pacific Seirra Research Corp.
1401 Wilson Boulevard
Arlington, VA 22209

Dr. Jeffrey W. Given
Sierra Geophysics
11255 Kirkland Way
Kirkland, WA 98033

Rong Song Jih
Teledyne Geotech
314 Montgomery Street
Alexandria, Virginia 22314

Professor F.K. Lamb
University of Illinois at
Urbana-Champaign
Department of Physics
1110 West Green Street
Urbana, IL 61801

Dr. Arthur Lerner-Lam
Lamont-Doherty Geological Observatory
of Columbia University
Palisades, NY 10964

Dr. L. Timothy Long
School of Geophysical Sciences
Georgia Institute of Technology
Atlanta, GA 30332

Dr. Peter Malin
University of California at Santa Barbara
Institute for Central Studies
Santa Barbara, CA 93106

Dr. George R. Mellman
Sierra Geophysics
11255 Kirkland Way
Kirkland, WA 98033

Dr. Bernard Minster
Institute of Geophysics and Planetary
Physics, A-205
Scripps Institute of Oceanography
Univ. of California, San Diego
La Jolla, CA 92093

Professor John Nabelek
College of Oceanography
Oregon State University
Corvallis, OR 97331

Dr. Geza Nagy
U. California, San Diego
Dept of Ames, M.S. B-010
La Jolla, CA 92093

Dr. Jack Oliver
Department of Geology
Cornell University
Ithaca, NY 14850

Dr. Robert Phinney/Dr. F.A. Dahlen
Dept of Geological
Geophysical Sci. University
Princeton University
Princeton, NJ 08540 (2 copies)

RADIX Systems, Inc.
Attn: Dr. Jay Pulli
2 Taft Court, Suite 203
Rockville, Maryland 20850

Dr. Norton Rimer
S-CUBED
A Division of Maxwell Laboratory
P.O. 1620
La Jolla, CA 92038-1620

Professor Larry J. Ruff
Department of Geological Sciences
1006 C.C. Little Building
University of Michigan
Ann Arbor, MI 48109-1063

Dr. Richard Sailor
TASC Inc.
55 Walkers Brook Drive
Reading, MA 01867

Thomas J. Sereno, Jr.
Service Application Int'l Corp.
10210 Campus Point Drive
San Diego, CA 92121

Dr. David G. Simpson
Lamont-Doherty Geological Observ.
of Columbia University
Palisades, NY 10964

Dr. Bob Smith
Department of Geophysics
University of Utah
1400 East 2nd South
Salt Lake City, UT 84112

Dr. S. W. Smith
Geophysics Program
University of Washington
Seattle, WA 98195

Dr. Stewart Smith
IRIS Inc.
1616 N. Fort Myer Drive
Suite 1440
Arlington, VA 22209

Rondout Associates
ATTN: Dr. George Sutton,
Dr. Jerry Carter, Dr. Paul Pomeroy
P.O. Box 224
Stone Ridge, NY 12484 (4 copies)

Dr. L. Sykes
Lamont Doherty Geological Observ.
Columbia University
Palisades, NY 10964

Dr. Pradeep Talwani
Department of Geological Sciences
University of South Carolina
Columbia, SC 29208

Dr. R. B. Tittmann
Rockwell International Science Center
1049 Camino Dos Rios
P.O. Box 1085
Thousand Oaks, CA 91360

Professor John H. Woodhouse
Hoffman Laboratory
Harvard University
20 Oxford St.
Cambridge, MA 02138

Dr. Gregory B. Young
ENSCO, Inc.
5400 Port Royal Road
Springfield, VA 22151-2388

OTHERS (FOREIGN)

Dr. Peter Basham
Earth Physics Branch
Geological Survey of Canada
1 Observatory Crescent
Ottawa, Ontario
CANADA K1A 0Y3

Dr. Eduard Berg
Institute of Geophysics
University of Hawaii
Honolulu, HI 96822

Dr. Michel Bouchon - Universite
Scientifique et Medicale de Grenob
Lab de Geophysique - Interne et
Tectonophysique - I.R.I.G.M-B.P.
38402 St. Martin D'Heres
Cedex FRANCE

Dr. Hilmar Bungum/NTNF/NORSAR
P.O. Box 51
Norwegian Council of Science,
Industry and Research, NORSAR
N-2007 Kjeller, NORWAY

Dr. Michel Campillo
I.R.I.G.M.-B.P. 68
38402 St. Martin D'Heres
Cedex, FRANCE

Dr. Kin-Yip Chun
Geophysics Division
Physics Department
University of Toronto
Ontario, CANADA M5S 1A7

Dr. Alan Douglas
Ministry of Defense
Blacknest, Brimpton,
Reading RG7-4RS
UNITED KINGDOM

Dr. Manfred Henger
Fed. Inst. For Geosciences & Nat'l Res.
Postfach 510153
D-3000 Hannover 51
FEDERAL REPUBLIC OF GERMANY

Dr. E. Husebye
NTNF/NORSAR
P.O. Box 51
N-2007 Kjeller, NORWAY

Ms. Eva Jonannisson
Senior Research Officer
National Defense Research Inst.
P.O. Box 27322
S-102 54 Stockholm
SWEDEN

Tormod Kvaerna
NTNF/NORSAR
P.O. Box 51
N-2007 Kjeller, NORWAY

Mr. Peter Marshall, Procurement
Executive, Ministry of Defense
Blacknest, Brimpton,
Reading FG7-4RS
UNITED KINGDOM (3 copies)

Dr. Ben Menaheim
Weizman Institute of Science
Rehovot, ISRAEL 951729

Dr. Svein Mykkeltveit
NTNF/NORSAR
P.O. Box 51
N-2007 Kjeller, NORWAY (3 copies)

Dr. Robert North
Geophysics Division
Geological Survey of Canada
1 Observatory crescent
Ottawa, Ontario
CANADA, K1A OY3

Dr. Frode Ringdal
NTNF/NORSAR
P.O. Box 51
N-2007 Kjeller, NORWAY

Dr. Jorg Schlittenhardt
Federal Inst. for Geosciences & Nat'l Res.
Postfach 510153
D-3000 Hannover 51
FEDERAL REPUBLIC OF GERMANY

University of Hawaii
Institute of Geophysics
ATTN: Dr. Daniel Walker
Honolulu, HI 96822

FOREIGN CONTRACTORS

Dr. Ramon Cabre, S.J.
c/o Mr. Ralph Buck
Economic Consular
American Embassy
APO Miami, Florida 34032

Professor Peter Harjes
Institute for Geophysik
Rhur University/Bochum
P.O. Box 102148, 4630 Bochum 1
FEDERAL REPUBLIC OF GERMANY

Professor Brian L.N. Kennett
Research School of Earth Sciences
Institute of Advanced Studies
G.P.O. Box 4
Canberra 2601
AUSTRALIA

Dr. B. Massinon
Societe Radiomana
27, Rue Claude Bernard
7,005, Paris, FRANCE (2 copies)

Dr. Pierre Mechler
Societe Radiomana
27, Rue Claude Bernard
75005, Paris, FRANCE

GOVERNMENT

Dr. Ralph Alewine III
DARPA/NMRO
1400 Wilson Boulevard
Arlington, VA 22209-2308

Dr. Robert Blandford
DARPA/NMRO
1400 Wilson Boulevard
Arlington, VA 22209-2308

Sandia National Laboratory
ATTN: Dr. H. B. Durham
Albuquerque, NM 87185

Dr. Jack Evernden
USGS-Earthquake Studies
345 Middlefield Road
Menlo Park, CA 94025

U.S. Geological Survey
ATTN: Dr. T. Hanks
Nat'l Earthquake Resch Center
345 Middlefield Road
Menlo Park, CA 94025

Dr. James Hannon
Lawrence Livermore Nat'l Lab.
P.O. Box 808
Livermore, CA 94550

Paul Johnson
ESS-4, Mail Stop J979
Los Alamos National Laboratory
Los Alamos, NM 87545

Ms. Ann Kerr
DARPA/NMRO
1400 Wilson Boulevard
Arlington, VA 22209-2308

Dr. Max Koontz
US Dept of Energy/DP 5
Forrestal Building
1000 Independence Ave.
Washington, D.C. 20585

Dr. W. H. K. Lee
USGS
Office of Earthquakes, Volcanoes,
& Engineering
Branch of Seismology
345 Middlefield Rd
Menlo Park, CA 94025

Dr. William Leith
USGS
Mail Stop 928
Reston, VA 22092

Dr. Richard Lewis
Dir. Earthquake Engineering and
Geophysics
U.S. Army Corps of Engineers
Box 631
Vicksburg, MS 39180

Dr. Robert Masse'
Box 25046, Mail Stop 967
Denver Federal Center
Denver, Colorado 80225

Richard Morrow
ACDA/VI
Room 5741
320 21st Street N.W.
Washington, D.C. 20451

Dr. Keith K. Nakanishi
Lawrence Livermore National Laboratory
P.O. Box 808, L-205
Livermore, CA 94550 (2 copies)

Dr. Carl Newton
Los Alamos National Lab.
P.O. Box 1663
Mail Stop C335, Group E553
Los Alamos, NM 87545

Dr. Kenneth H. Olsen
Los Alamos Scientific Lab.
Post Office Box 1663
Los Alamos, NM 87545

Howard J. Patton
Lawrence Livermore National
Laboratory
P.O. Box 808, L-205
Livermore, CA 94550

Mr. Chris Paine
Office of Senator Kennedy
SR 315
United States Senate
Washington, D.C. 20510

AFOSR/NP
ATTN: Colonel Jerry J. Perrizo
Bldg 410
Bolling AFB, Wash D.C. 20332-6448

HQ AFTAC/TT
Attn: Dr. Frank F. Pilotte
Patrick AFB, Florida 32925-6001

Mr. Jack Rachlin
USGS - Geology, Rm 3 C136
Mail Stop 928 National Center
Reston, VA 22092

Robert Reinke
AFWL/NTESG
Kirtland AFB, NM 87117-6008

HQ AFTAC/TGR
Attn: Dr. George H. Rothe
Patrick AFB, Florida 32925-6001

Donald L. Springer
Lawrence Livermore National Laboratory
P.O. Box 808, L-205
Livermore, CA 94550

Dr. Lawrence Turnbull
OSWR/NED
Central Intelligence Agency
CIA, Room 5G48
Washington, D.C. 20505

Dr. Thomas Weaver
Los Alamos Scientific Laboratory
Los Almos, NM 97544

AFGL/SULL
Research Library
Hanscom AFB, MA 01731-5000 (2 copies)

Secretary of the Air Force (SAFRD)
Washington, DC 20330
Office of the Secretary Defense
DDR & E
Washington, DC 20330

HQ DNA
ATTN: Technical Library
Washington, DC 20305

DARPA/RMO/RETRIEVAL
1400 Wilson Blvd.
Arlington, VA 22209

DARPA/RMO/Security Office
1400 Wilson Blvd.
Arlington, VA 22209

AFGL/XO
Hanscom AFB, MA 01731-5000

AFGL/LW
Hanscom AFB, MA 01731-5000

DARPA/PM
1400 Wilson Boulevard
Arlington, VA 22209

Defense Technical
Information Center
Cameron Station
Alexandria, VA 22314
(5 copies)

Defense Intelligence Agency
Directorate for Scientific &
Technical Intelligence
Washington, D.C. 20301

Defense Nuclear Agency/SPSS
ATTN: Dr. Michael Shore
6801 Telegraph Road
Alexandria, VA 22310

AFTAC/CA (STINFO)
Patrick AFB, FL 32925-6001

Dr. Gregory van der Vink
Congress of the United States
Office of Technology Assessment
Washington, D.C. 20510

Mr. Alfred Lieberman
ACDA/VI-OA'State Department Building
Room 5726
320 - 21St Street, NW
Washington, D.C. 20451

TACTEC
Battelle Memorial Institute
505 King Avenue
Columbus, OH 43201 (Final report only)